



# Aerogel-derived nickel-iron oxide catalysts for oxygen evolution reaction in alkaline media

Luigi Osmieri<sup>a,\*</sup>, Haoran Yu<sup>b</sup>, Raphaël P. Hermann<sup>c</sup>, Melissa E. Kreider<sup>d</sup>, Harry M. Meyer III<sup>e</sup>, A. Jeremy Kropf<sup>f</sup>, Jae Hyung Park<sup>f</sup>, Shaun M. Alia<sup>d</sup>, David A. Cullen<sup>b</sup>, Deborah J. Myers<sup>f</sup>, Piotr Zelenay<sup>a,\*</sup>

<sup>a</sup> MPA-11, Materials Physics and Applications Division, Los Alamos National Laboratory, Los Alamos, NM 87545, USA

<sup>b</sup> Center for Nanophase Materials Sciences, Oak Ridge National Laboratory, Oak Ridge, TN 37830, USA

<sup>c</sup> Materials Science and Technology Division, Oak Ridge National Laboratory, Oak Ridge, TN 37830, USA

<sup>d</sup> Chemical and Material Sciences Center, National Renewable Energy Laboratory, Golden, CO 80401, USA

<sup>e</sup> Chemical Sciences Division, Oak Ridge National Laboratory, Oak Ridge, TN 37830, USA

<sup>f</sup> Chemical Sciences and Engineering Division, Argonne National Laboratory, Lemont, IL 60439, USA

## ARTICLE INFO

### Keywords:

Water electrolysis  
Anion exchange membrane  
Oxygen evolution reaction  
Aerogel  
Nickel-iron (oxy)hydroxide

## ABSTRACT

Anion exchange membrane water electrolyzers (AEMWEs) can generate hydrogen with a pure water feed using noble metal-free catalysts. The development of highly active and stable catalysts for oxygen evolution reaction (OER) is required for improving performance of AEMWEs systems. Ni-Fe (oxy)hydroxides show high OER catalytic activity in alkaline media, but typically have low surface area. In this work, we investigate a series of Ni-Fe oxides with high surface area and disordered morphology, obtained using an aerogel synthesis method. We evaluate the impact of different synthesis variables on the OER activity and demonstrate that heat treatment at high temperatures generates more ordered structure, resulting in a decrease in OER activity. Advanced characterization reveals that maintaining highly disordered and porous structure of the aerogel is essential to achieving high OER activity, as it enables the formation of highly OER-active lamellar structures of the catalyst.

## 1. Introduction

The energy-sector decarbonization is the main strategy adopted by many governments worldwide to mitigate global climate change [1,2]. The amount of electricity generated via renewable sources has been increasing over the last decade, becoming a promising way to achieve the decarbonization goal [3]. Unfortunately, the availability of many sources of renewable energy (e.g., solar, wind, tide) is intermittent and does not necessarily match the electricity consumption peaks, thus requiring means for energy storage [4]. Generating hydrogen (H<sub>2</sub>) using the excess renewable electricity, and storing and distributing it to generate electricity when and where it is needed can facilitate reaching decarbonization goals [5]. Hydrogen generated by water electrolysis using renewable electricity is defined as “green”, meaning it is formed without emitting greenhouse gases [6–8]. Low temperature water electrolysis (LTWE) is an attractive technology for green H<sub>2</sub> generation at close to ambient temperature (less than 100 °C), enabling fast

start-up/shut-down, and implementation on a relatively small scale, e.g., portable and residential applications [9,10].

Currently, the two LTWE technologies which are widely commercialized are liquid alkaline water electrolyzers (LAWEs) and proton exchange membrane water electrolyzers (PEMWEs) [9,11,12]. LAWEs require highly concentrated and corrosive alkali solutions (> 4 M KOH) and operate at low current densities, typically ca. 0.5–0.75 A cm<sup>−2</sup> [13]. LAWEs operate without a solid polymer electrolyte, i.e., a membrane, and have the advantage of using inexpensive Ni-based catalysts [14,15]. On the other hand, PEMWEs operate on pure water and allow for reaching high current densities, 2 A cm<sup>−2</sup> or higher [16,17]. However, due to the highly acidic environment created by the perfluorosulfonic acid polymer electrolyte membranes and ionomer used in the electrodes (i.e., Nafion™), they need expensive platinum group metal (PGM)-based electrocatalysts [18–20]. In particular, Pt-based catalysts are used at the cathode for the hydrogen evolution reaction (HER), and Ir-based ones at the anode for the oxygen evolution reaction (OER) [17]. Due to the

\* Corresponding authors.

E-mail addresses: [losmieri@lanl.gov](mailto:losmieri@lanl.gov) (L. Osmieri), [zelenay@lanl.gov](mailto:zelenay@lanl.gov) (P. Zelenay).

<https://doi.org/10.1016/j.apcatb.2024.123843>

Received 16 October 2023; Received in revised form 30 January 2024; Accepted 12 February 2024

Available online 14 February 2024

0926-3373/© 2024 Elsevier B.V. All rights reserved.

complexity of OER mechanism, involving four electron/proton transfer steps [21], and the lack of a stable electronically conducting support to allow dispersion of Ir catalysts, PEMWEs require high Ir loadings at the anode [20,22]. The extremely low relative abundance of Ir on the Earth's crust, and, as a consequence, the extremely high price of the metal, ca. 4700 U.S. \$/oz (October 2023) [23], are important factors impacting widespread commercialization of PEMWE systems [24].

Recently, significant breakthroughs in the development of commercial anion exchange membrane (AEM) materials have opened the way for a new LTWE technology: the anion exchange membrane water electrolyzer (AEMWE) [25–28]. Research in the AEMWE field is gaining momentum since successful development of this class of electrolyzers can result in combining the advantages of LAWE and PEMWE, that is, paving the path for operation on pure water (or with KOH concentration much lower than in LAWEs) at high current densities and with PGM-free catalysts [9,14,29,30].

The use of carbon-based catalysts in the electrolyzer anode could be advantageous due to high surface area (typically from 200 to more than 1000 m<sup>2</sup> g<sup>−1</sup>) and electronic conductivity [31–33] of carbon materials. These advantages are outweighed, however, by the propensity of carbons for corrosion at high potentials of the anode operation [34–36]. At low pH's, the OER catalyst of possibly the only choice for is IrO<sub>2</sub>. At high pH's, i.e., for AEMWEs, the choice broadens onto various transition-metal oxides and mixed oxides (e.g., spinels, perovskites) [37–39], as well as chalcogenides, phosphides and nitrides [40], which have shown good OER activity and stability in alkaline media. In particular, OER catalysts based on Ni in the form of oxides, hydroxides, and oxyhydroxides, have shown promising performance in alkaline media [41–44]. Ni hydroxide, Ni(OH)<sub>2</sub>, occurs in different forms denoted as α-Ni(OH)<sub>2</sub> and β-Ni(OH)<sub>2</sub>, with several possible types of structural disorder [45–47]. Doping these materials with Fe dramatically improves their OER activity, as demonstrated in the literature [38,48–51]. However, the Ni-Fe (oxy)hydroxides seem to suffer from low electronic conductivity compared to other metal oxide-based OER catalysts (e.g., Co<sub>3</sub>O<sub>4</sub>, IrO<sub>2</sub>), which may be the cause of their poor electrolyzer performance [52]. Due to the presence of multiple phases and surface terminations, transitional charging-discharging behavior [43,46,53–55], the OER mechanism at Ni-Fe (oxy)hydroxides and, in particular, the role of Fe-doping in enhancing the OER activity in Ni-based (oxy)hydroxides, as well as the oxidation states of Ni and Fe (and their variation) during the OER, have been subject of an ongoing debate in the literature [41,42,51,56,57].

Transition metal-oxide OER catalysts for alkaline media tend to have low surface areas, from 5 to 50 m<sup>2</sup> g<sup>−1</sup> [29,30,58], which may limit their performance. Several different methods for the synthesis of Ni- and Ni-Fe (oxy)hydroxides have been reported [46], including sol-gel synthesis combined with drying in supercritical CO<sub>2</sub> [59]. Recent modification of the latter approach by an addition of Fe has resulted in aerogel-like Ni-Fe oxides with promising OER activity in alkaline media [48], though not yet confirmed in an operating AEMWE (unlike that of other types of Ni-Fe-based catalysts) [11,52,60–65]. The synthesis of transition metal oxides and hydroxides using the aerogel method offers a considerable potential advantage over other synthesis methods, as it allows to overcome the low surface-area challenge, typical for these materials. The gel drying process (supercritical drying [59,66] or freeze-drying [67,68]) enables solvent removal while maintaining the finely dispersed oxide/hydroxide structure as in the gel matrix. During the process, the solvent removal yields a highly porous structure which is responsible for the high surface area, characteristic of oxide/hydroxide aerogels [48,59,66,69].

In this work, we synthesized several Ni-Fe oxide-based materials using a modified version of the previously proposed aerogel synthesis approach [48,59]. We explored the impact of various synthesis variables on the OER activity, including that of heat-treatment temperature, Ni-to-Fe molar ratio, and addition of a third transition metal (Co, Mn). We characterized the materials before testing and utilized one of the

most promising catalysts in an AEMWE, assessing its performance with pure-water and supporting-electrolyte feeds. Finally, we characterized the materials after testing, showing that the most active catalyst underwent a substantial structural modification during testing that highlights an important correlation between the initial structural disorder in the catalyst and its high OER activity in the AEMWE anode.

## 2. Experimental

### 2.1. Catalysts synthesis

The transition metal oxide aerogels were prepared using a previously proposed method [48,59,69], with some modifications. NiCl<sub>2</sub>•6 H<sub>2</sub>O (Fisher Scientific), FeCl<sub>2</sub>•4 H<sub>2</sub>O, CoCl<sub>2</sub>•6 H<sub>2</sub>O, MnCl<sub>2</sub>•4 H<sub>2</sub>O (Sigma Aldrich) and 30 mg of polyacrylic acid (MW 450,000, Sigma Aldrich) were dissolved in 17.5 mL of ethanol (200 proof, Sigma Aldrich) while stirred in a glass vial. The total moles of transition metal salts were kept constant at 7.813 mmol, and the amount of each salt was varied according to the desired nominal composition. Once complete dissolution was achieved, typically after 30 minutes, the solution was transferred into a plastic vial and 2 mL of propylene oxide (PO) was slowly added at a rate of ca. 1 mL min<sup>−1</sup>. The vial was sealed and left to age for 48 hours. Fig. S1a in Supplementary Information shows an appearance of some gels after the aging step. Approximately 40 mL of ethanol was then added to the vial and ethanol was replaced several times a day over the course of at least three days to ensure thorough gel washing. The gel was then transferred into a stainless-steel sample holder equipped with a fine 2 μm metal grid and inserted into the chamber of an automated supercritical CO<sub>2</sub> dryer (Autosamdri-931, Tousimis, USA), initially filled with ethanol. The supercritical drying process consisted of five cycles of purging with liquid CO<sub>2</sub> followed by a three-hour dwell time, with a final step of holding at supercritical conditions (38 °C and 82 bar) for two hours. The aerogels were then heat-treated under air atmosphere in a tube furnace for 3 h. Two different heat-treatment temperatures were used, 150 °C and 500 °C. Fig. S1b shows the appearance of two different aerogels, NiFe8:1 and NiFe2:1, after drying and after the heat treatment at 150 °C and 500 °C. To further investigate the effect of the heat treatment temperature, samples heat-treated at 75 °C and 300 °C starting from the NiFe8:1 aerogel were also prepared. The catalysts will be referred to as NiFeX:Y-T, where X:Y is the Ni-to-Fe molar ratio, and T is the heat treatment temperature (in °C).

### 2.2. Physical and chemical characterization

#### 2.2.1. BET surface area and pore size distribution

The surface area and pore size distribution of selected aerogels after heat treatment at 150 °C and 500 °C were measured with a Quantachrome Autosorb-iQ at 77 K in liquid N<sub>2</sub>. Before the analysis, samples were placed in a glass sample tube and degassed under vacuum for 3 h at 150 °C. The surface area was calculated using the Brunauer–Emmett–Teller (BET) method in the relative pressure range of 0.05 and 0.3. The pore volume and size distribution were obtained using a density functional theory (DFT) method included in the instrument software.

#### 2.2.2. XRD

X-ray diffraction (XRD) patterns were collected to determine crystallographic structure of several catalysts before and after testing in an AEMWE. The measurements utilized a Siemens D5000 diffractometer using a Cu K<sub>α</sub> radiation source and a graphite monochromator. Diffraction patterns were recorded in the 2θ range between 20 and 90°, with a 0.1° step. The Jade9 software was used to determine the crystallographic phases associated with the peaks in the XRD patterns.

#### 2.2.3. XPS

X-ray photoelectron spectroscopy (XPS) characterization was performed using a Thermo Scientific (Waltham, MA, USA) Model K-Alpha.

The instrument utilized monochromated, micro-focused, Al  $K_{\alpha}$  X-rays (1486.6 eV) with a variable spot size (i.e., 30–400  $\mu\text{m}$ ). A 400  $\mu\text{m}$  X-ray spot size was used for maximum signal and to obtain an average surface composition over the largest possible area. The instrument was equipped with a hemispherical electron energy analyzer with a 128-channel detector system. The base pressure in the analysis chamber was typically  $2 \times 10^{-9}$  mbar or lower. Samples for analysis were prepared by dispersing the powder material onto double-sided tape fixed to clean glass slides. Sufficient material was used to prevent any interfering signals from the tape. After transferring the sample into the analysis chamber, a survey spectrum (step size 1 eV, pass energy 200 eV) was acquired to determine all elements present. Next, high-resolution core level spectra were acquired for detailed chemical state analysis, using step size of 0.1 eV and pass energy of 50 eV. C KLL (Auger) spectra were obtained using a step size of 2 eV and a pass energy of 100 eV. All spectra were acquired with the charge neutralization flood gun, a combination of low energy electrons and Ar ions, under a stable analysis condition. The typical pressure in the analysis chamber with the flood gun operating was  $2 \times 10^{-7}$  mbar. Data were collected and processed using the Thermo Scientific Avantage XPS software package (v.5.96).

#### 2.2.4. STEM-EDS-EELS

The morphology and composition of catalysts were determined via aberration-corrected scanning transmission electron microscopy (STEM) using a JEOL NEOARM (JEOL Ltd.) and equipped with dual 100 mm<sup>2</sup> solid state detectors for energy dispersive X-ray spectroscopy (EDS). Secondary electron (SE) and high-angle annular dark-field (HAADF) images were recorded simultaneously at 80 kV using the DigitalMicrograph software (Gatan, Inc.). Electron energy-loss spectroscopy (EELS) was obtained at 200 kV and the data analyzed using custom Python code. Atomic-resolution STEM-EDS maps were acquired and processed in the JEOL Analysis Station software (JEOL Ltd.) using the standard-less Cliff-Lorimer routine.

#### 2.2.5. X-ray absorption spectroscopy

X-ray absorption spectroscopy (XAS) data at the Fe and Ni K edges were acquired to determine the oxidation state and atomic structure of the Ni and Fe in the as-prepared NiFe8:1, the NiFe8:1 heat-treated to 150 °C, the NiFe8:1 heat-treated to 500 °C, and these last two materials after testing in an AEMWE. The spectra were acquired at beam line 10-ID at Argonne National Laboratory's Advanced Photon Source in both transmission and fluorescence modes from 6930 eV to 7900 eV (Fe K edge) and from 8132 eV to 9182.3 eV (Ni K edge), using Ar gas ionization chambers with a Mn filter for the Fe edge and a Co filter for the Ni edge and Soller slits in the Stern-Heald geometry. The second derivative of the XAFS spectrum of Ni and Fe foils, located downstream of the samples, was used to calibrate the Fe K-edge energy to 7110.75 eV and the Ni K-edge energy to 8331.37 eV. Spectra were also acquired for a series of Ni oxide and Ni hydroxide standards and Fe oxide and Fe hydroxide standards for comparison with the spectra for the NiFe8:1 catalyst.

#### 2.2.6. Mössbauer spectroscopy

Powder <sup>57</sup>Fe transmission Mössbauer spectra were obtained using a Wissel GmbH constant acceleration drive in the 12–4 mm/s range (for magnetic and paramagnetic spectra, respectively). The optimized loading of the NiFe8:1 catalyst for <sup>57</sup>Fe Mössbauer spectroscopy ranged from 27 to 34 mg cm<sup>-2</sup>, depending on the oxygen content. We used a sample with 30 mg cm<sup>-2</sup>, i.e., 37 mg material in a 12.5 mm diameter sample holder, both for the NiFe8:1–150 and NiFe8:1–500 samples. The source was ~1 mCi <sup>57</sup>Co in Rh foil. The sample was placed in a Janis SHI-850 closed cycle cryostat and a Tl@NaI scintillator was used. The drive was calibrated using Fe foil at a room temperature, which also served as reference for the isomer shift. An additional spectrum was measured at room temperature in the 2.5 mm s<sup>-1</sup> range using a similar drive and procedure, with a Kr gas proportional counter.

### 2.3. Electrochemical characterization

#### 2.3.1. Testing in three-electrode cell

To assess OER activity, the catalyst powder (5 mg of catalyst per mL of dispersion) was dispersed in into a mixture of deionized (DI) water (Milli-Q, > 18 M $\Omega$  cm resistivity) and isopropanol (IPA) with a 2:1 DI water-to-IPA volume ratio. D521 Nafion™ ionomer dispersion (5 wt%, equivalent weight 1100 g eq<sup>-1</sup>, Ion Power) was also added to the mixture as a binder, at an amount that assured an ionomer-to-catalyst mass ratio of 0.2, to prevent the catalyst detachment from the electrode during testing. To avoid possible corrosion of the catalyst powder due to the Nafion™ ionomer acidity, the ionomer dispersion was earlier neutralized with 1 M NaOH [70]. An aliquot of the catalyst dispersion necessary to achieve the desired catalyst loading, typically 0.25 mg cm<sup>-2</sup>, was then drop-casted using a micropipette onto the tip of an Au working electrode. A reversible hydrogen electrode (RHE) was used as the reference electrode, and a graphite rod was used as the counter electrode. The RHE was made in-house using a plastic case equipped with a porous polypropylene frit. A platinized platinum wire, and two pieces of PTFE tubes (to allow H<sub>2</sub> gas in and out) were inserted in the case and the case cap was sealed. H<sub>2</sub> gas was continuously flowing through the reference electrode during the experiments. The electrolyte solution was 0.1 M KOH saturated with N<sub>2</sub> gas. The solution was prepared by dissolving in DI water KOH pellets (Sigma Aldrich ACS reagent grade purity). The electrochemical test was carried out with a rotating disk electrode (RDE) cell setup (Pine Research, USA) and a BioLogic SP-300 potentiostat. A PTFE cell was used to avoid any possible corrosion of glass components in contact with the alkaline electrolyte.

To condition and activate the catalyst, cyclic voltammetry (CV) was performed at 50 mV s<sup>-1</sup> between 0.05 and 1.65 V vs. RHE. CV cycles were recorded until a stable profile was obtained, typically after 20 cycles, but for at least 10 cycles. Then, 5 CV cycles were recorded at 10 mV s<sup>-1</sup> between 1.20 and 1.80 V vs. RHE, followed by recording staircase voltammetry (SV) plot in the same potential range in both forward and backward scan direction, using 10-mV potential step and 10 s hold time. In all these experiments the RDE rotation speed was 1600 rpm to facilitate removal of O<sub>2</sub> bubbles generated at the working electrode. Electrochemical impedance spectroscopy (EIS) was acquired in a potentiostatic mode at open circuit potential and in a galvanostatic mode at 10 mA cm<sup>-2</sup> in the frequency range from 100 kHz to 1 Hz. The high frequency resistance (HFR), determined as the intercept with the real axis of the EIS Nyquist plot was used to correct the SV polarization curves for the ohmic (iR) contribution. Some RDE experiments were conducted with different rotation speeds, in the range between 400 and 2500 rpm, to assess the impact of rotation speed on OER performance. OER stability experiments were conducted under the conditions described above at a current density of 10 mA cm<sup>-2</sup> for 54 h. SV polarization curves and EIS plots were recorded before and after the current hold.

#### 2.3.2. Membrane electrode assembly (MEA) preparation

To test performance of select catalysts in an operating the water electrolyzer, MEAs were prepared at Los Alamos National Laboratory (LANL) using the method as described in detail in our previous work [30]. A commercial PtRu/C catalyst (Pt 40%, Ru 20% on carbon black, HiSPEC™ 10000, Alfa Aesar) was used at the cathode. The catalyst was mixed with DI water, IPA, and a commercial anion exchange ionomer (PiperION-A5-HCO3EtOH, 5 wt%, equivalent weight 425.5 g eq<sup>-1</sup>, Versogen) to form an ink which was deposited onto a 5 cm<sup>2</sup> piece of carbon paper (MGL370, AvCarb) using a SonoTek ultrasonic spray coating system, controlling the loading to 1 mg<sub>Pt</sub> cm<sup>-2</sup>. For the anode, two different commercial porous transport layer (PTL) materials were used: platinized sintered Ti (Giner Inc., USA) and Ni foam (Stanford Advanced Materials, USA). To prepare the Ni-foam PTL, two pieces of the original material were pressed together at 100 kg cm<sup>-2</sup> for 5 minutes. For the anode catalyst ink preparation, neutralized D521 Nafion

ionomer dispersion was also added to act as binder and prevent the partial catalyst detachment from the electrode when exposed to DI water [30]. The ratio between the mass of the PiperION anion exchange ionomer and the catalyst was 0.77 and the Nafion-to-PiperION equivalent ratio was 0.16. The catalyst ink was sprayed onto a 5 cm<sup>2</sup> PTL piece as described before, controlling the catalyst loading to 1.5 mg cm<sup>-2</sup>. The appearance of the PTL materials before and after the catalyst ink deposition is shown in Fig. S2 (left and center). Before testing, both the anode- and cathode-catalyst-coated substrates (CCS's) were immersed into 1 M NaOH solution overnight to ion-exchange the ionomer from the original HCO<sub>3</sub><sup>-</sup>-form to the OH<sup>-</sup>-form, suitable for AEMWE testing. For the MEA fabrication, a piece of commercial AEM (PiperION-A40-HCO<sub>3</sub>, Versogen) was used. Prior to use, the AEM was treated in 1 M NaOH for ion exchange for 2 h (replacing the solution after the first hour) and then rinsed with abundant DI water until neutral pH was achieved. The MEA was assembled by placing the anode and cathode CCS on the opposite sides of the AEM (without hot pressing) inside the cell hardware. A fiber-reinforced PTFE gasket (250 μm thickness) was used at each side of the cell, and the cell bolts were tightened at 8.5 Nm.

For the durability testing in 1 M KOH, the MEAs were prepared at the National Renewable Energy Laboratory (NREL). A commercial Pt/C catalyst (47% Pt, Tanaka Kikinzoku Kogyo, TEC10E50E) was used at the cathode. The catalyst ink was made with 57% DI water, 43% nPA, and a commercial anion exchange ionomer (PiperION-A TP-85, 5 wt%, Versogen) with a catalyst ink concentration of 5.7 mg mL<sup>-1</sup> and an ionomer-to-catalyst mass ratio of 0.3. The cathode ink was airbrush-sprayed onto a 5 cm<sup>2</sup> carbon paper (Fuel Cell Earth, MGL280, 80280–40) mounted to a vacuum hot plate at 80 °C. The inks for both anode materials, our NiFe8:1–150 catalyst and commercial NiFe<sub>2</sub>O<sub>4</sub> (US Research Nanomaterials, 98%), were prepared by mixing the catalyst powder with the solvent (a mixture of 90% nPA and 10% DI water) and the PiperION-A TP-85 ionomer. The ionomer-to-catalyst mass ratio was 0.3. The anode ink was airbrush-sprayed onto a 5 cm<sup>2</sup> Ni fiber PTL (Bekaert, BEKIPOR 2Ni 18–0.25) mounted to a vacuum hot plate at 80 °C. The target catalyst loadings of 0.3 and 1 mg cm<sup>-2</sup> (metal basis) for the cathode and anode, respectively, were confirmed with X-ray fluorescence (Fischer XDV-SDD XRF). For ion exchange before testing, the PiperION-A TP-85 (Versogen, 80 μm) membrane was soaked in 3 M KOH (EMD Millipore, Emsure grade) for 48 h, with the solution refreshed after 24 h, and the electrodes were soaked in 3 M KOH for 1 h. The 25 cm<sup>2</sup> hardware consisted of Al endplates (Fuel Cell Technologies), Au current collectors, and Ni triple serpentine flow fields. PTFE gaskets (280 μm thickness) were used at the cathode and anode to achieve contact between the MEA components and approximately 20% compression on the GDL at 4.5 Nm.

### 2.3.3. Water electrolyzer testing

Before starting AEMWE polarization measurements at LANL, DI water was passed through the anode cell compartment at a flow rate of 10 mL min<sup>-1</sup>, and the cell temperature was set to 70 °C, using an electronic metering pump (Pulsatron). The cell temperature was controlled using a digital controller equipped with a thermocouple (Fuel Cell Technologies, Inc.). During operation, the DI water was recirculated from the outlet to the inlet of the cell by passing through a 1 L tank that allowed for degassing of the O<sub>2</sub> generated at the anode. The H<sub>2</sub> generated at the cathode was vented after passing through a water trap. The polarization curves were recorded in a current-control mode using a BioLogic VMP3 potentiostat with a VMP3B-20 20 A current booster. Following the procedure described previously for the MEA activation [27,30], consecutive polarization curves were recorded between 0.1 and 1.0 A cm<sup>-2</sup> in 0.1 A cm<sup>-2</sup> increments, using 3-minute holds at each current value. The polarization curve measurements were repeated until a stable curve profile was obtained, after 3–10 times depending on the anode catalyst. For the full polarization curve measurement, the current was increased in 0.1 A cm<sup>-2</sup> increments in the 0.1–1.0 A cm<sup>-2</sup> range and in 0.2 A cm<sup>-2</sup> increments in the 1.0–2.0 A cm<sup>-2</sup> range, using 3-minute

holds and voltage recording every 0.5 s. The voltage values measured over the last 30 s of each step were averaged to calculate the polarization curve points. To determine HFR at different current densities, multiple EIS were recorded in a galvanostatic mode between 0 and 1 A cm<sup>-2</sup> in 0.1 cm<sup>-2</sup> increments, with AC amplitude of 5% of the current value in the 100 kHz to 1 Hz range. After measurements with DI water feed, ca. 200 mL of 1% K<sub>2</sub>CO<sub>3</sub> solution was passed through the anode and consecutive polarization curves in 1% K<sub>2</sub>CO<sub>3</sub> solution were recorded until stable response was achieved. Following EIS measurements, the anode was flushed with ca. 500 mL of DI water and ca. 200 mL of 0.1 M KOH solution, and consecutive polarization curves and EIS measurements were performed in recirculating 0.1 M KOH solution. The fabrication and testing procedure for the AEMWE MEA with IrO<sub>2</sub> catalyst at the anode, shown for the purpose of comparison in Fig. S4, and for the PEMWE MEA, have been described previously [30].

The durability testing performed at NREL was carried out in a 1 M KOH supporting electrolyte (EMD Millipore, Emsure grade) at 80 °C with a flow rate of 50 mL min<sup>-1</sup> to the anode and cathode, using an Autolab PGSTAT302N potentiostat and a 20 A booster (Eco Chemie, Metrohm Autolab). The cell was conditioned via a 2-h hold at 2 V, followed by a polarization curve measured using constant-voltage holds for 2 minutes at 1.4 V and 2 V. EIS measurements were performed at these voltages, as well as at non-Faradaic voltages between 1.25 and 1.35 V. The frequency range was 18 kHz to 0.1 Hz. Durability was assessed in a 110-h galvanostatic measurement at 1 A cm<sup>-2</sup> using an HP 6031 A power supply.

## 3. Results and discussion

### 3.1. Electrochemical characterization in RDE

The OER electrocatalytic activity and other electrochemical properties of aerogel-derived catalysts were tested using an RDE setup. We conducted a preliminary set of experiments with the goal of optimizing the catalyst loading on the RDE tip and the rotation speed. The results are shown in Fig. S5. Loading had been found to influence catalytic activity measured with RDE setups, among others, for oxygen reduction reaction [71,72]. Other groups have investigated by RDE the impact of catalyst loading on the OER in alkaline media, finding that the electrode substrate can play a role as well [73,74]. In this work, we recorded cyclic voltammograms (Fig. S5a) and determined iR-corrected OER activity (Fig. S5b) of an NiFe 8:1 aerogel catalyst heat-treated in air at 150 °C, deposited on an Au RDE tip. Hereinafter this catalyst will be referred to as NiFe8:1–150. We used five different loadings, from 0.05 mg cm<sup>-2</sup> up to 1 mg cm<sup>-2</sup>. The CVs in Fig. S5a show an increase in the redox peak areas in both the anodic and the cathodic scan directions upon an increase in the loading from 0.05 to 0.25 mg cm<sup>-2</sup>. However, when loading is increased even more, to 0.5 and 1 mg cm<sup>-2</sup>, the intensity of the peaks drastically decreases. The presence of these redox peaks is associated with a redox transition from Ni(II) in Ni(OH)<sub>2</sub> to Ni(III) in NiOOH [41,50,75], according to the reaction: Ni(OH)<sub>2</sub> + OH<sup>-</sup> ⇌ NiOOH + H<sub>2</sub>O + e<sup>-</sup>. Steady-state SV measurements helps to minimize capacitive and pseudocapacitive contributions to these peaks enabling the detection of the pure faradaic component associated with the OER. Polarization curves in Fig. S5b expose current dependence on the catalyst loading, with the best performance reached with the 0.25 mg cm<sup>-2</sup> loading. After the subtraction of the iR component due to the ohmic resistance of the electrolyte solution and the electronic resistance of the electrode and cables, the electrocatalytic OER activity can be visualized. The ohmic resistance measured by EIS was between 8 and 9 Ω cm<sup>2</sup> in these tests. The results suggest that the lowest OER overpotential is reached with the 0.25 mg cm<sup>-2</sup> loading. Within the range of catalyst loadings explored, we observed a difference in OER activity, measured as an iR-free potential at a current density of 10 mA cm<sup>-2</sup>, of up to ca. 40 mV (inset in Fig. S5b).

Therefore, OER electrocatalysis experiments are commonly carried



out in RDE cells [38,48,70,76–79]. The benefit of using an RDE setup is that the rotation of the working electrode helps the removal of the bubbles of  $O_2$  gas generated during the experiment. In the next of two preliminary steps, we assessed whether the rotation speed played a role in the OER studies. We performed SV measurements using the optimal catalyst loading of  $0.25 \text{ mg cm}^{-2}$  and at four different rotation speeds: 400, 900, 1600, and 2500 rpm (Fig. S5c). The difference in the iR-free potentials at  $10 \text{ mA cm}^{-2}$  was within 6 mV for the forward (anodic) scan direction (inset in Fig. S5c) and slightly more (10 mV) for the backward (cathodic) scan. The worst performance was measured at 400 rpm, especially at high potentials, at which the formation gas of gas bubbles is correspondingly more intense. Given very small difference in OER potentials at  $10 \text{ mA cm}^{-2}$  in 900 and 1600 rpm tests (3 mV), we ultimately decided to use 1600 rpm speed in the follow-up experiments to assure effective removal of the bubbles.

After these preliminary tests, we measured the OER activity of other aerogel-derived catalysts, exploring some of the synthesis variables. First, we investigated the impact of two heat-treatment temperature, 150 and 500 °C. We examined the aerogel-derived catalysts synthesized using a Ni-to-Fe ratio of 8:1 and 2:1 (catalysts named NiFe2:1–150 and NiFe2:1–500). The results are shown in Fig. 1a–b. From CVs in Fig. 1a we can see that both the catalysts heat-treated at 150 °C have well defined redox peaks reflecting the Ni(II) to Ni(III) transition. For the catalyst with higher Fe content the peaks are shifted towards more positive potentials. This shift is more evident in the negative scan direction, while in the positive direction the peak overlaps with the OER current (having an onset potential of ca. 1.45 V vs. RHE). We define the OER onset potential as a potential at which a current density of  $1 \text{ mA cm}^{-2}$  is measured in the steady-state SV experiment. The Ni(II)  $\rightleftharpoons$  Ni(III) redox peak is not seen in the CV of the catalyst heat-treated at 500 °C. The catalysts heat-treated at the higher temperature do not show any pseudocapacitive signatures at potentials below the OER onset. Also, the double-layer capacitive current measured with these catalysts is much smaller than measured with catalysts heat-treated at 150 °C. The iR-corrected SVs in Fig. 1b allow to better visualize OER activity. The two catalysts heat-treated at 150 °C show almost identical OER performance, with onset potential of ca. 1.43 V vs. RHE and a current density of  $10 \text{ mA cm}^{-2}$  at ca. 1.50 V vs. RHE. The large difference in their Fe content, as well as the difference in the CV redox peaks does not result in a substantial difference in OER activity for these catalysts. The two catalysts heat-treated at 500 °C show a much lower OER activity, with of 90 mV to 120 mV differences in the OER onset potential and iR-corrected potential at  $10 \text{ mA cm}^{-2}$  compared to the corresponding values measured with catalysts heat-treated at 150 °C. The NiFe2:1–500 catalyst shows better performance than the NiFe8:1–500 by ca. 40 mV at  $10 \text{ mA cm}^{-2}$ , which can be related to the formation of a higher number of Ni-Fe active sites in this catalyst, possibly thanks to its higher surface area and pore volume (see Table 1). Another reason could be better electronic conductivity which can be induced by the higher Fe content [50].

To investigate more in depth the effect of the heat treatment temperature and verify if higher OER activity could be obtained with a heat treatment temperature between 150 and 500 °C, we synthesized a catalyst heat-treated at 300 °C using the NiFe8:1 aerogel. The results are shown in Fig. S6. Redox peaks are still observed in the CV of the catalyst heat-treated at 300 °C, but with reduced intensity compared to the catalyst heat-treated at 150 °C, and its OER activity is intermediate between the catalysts heat treated at 150 °C and at 500 °C.

We investigated the impact of the Fe content in the catalyst synthesis, comparing a sample containing only Ni with four samples with different Ni-to-Fe ratios: 2:1, 4:1, 8:1, and 16:1. All the samples in this case were subjected to heat treatment at 150 °C, which yielded much more active than materials heat-treated at 500 °C (see above). Fig. 1c depicts CVs for these five materials. Fe content gives rise to bigger CV redox peaks than observed with samples containing only Ni. For the samples containing Fe, a lower Fe content corresponds to larger redox peaks area, and lower

peak potentials. This peak potential shift is more evident in the cathodic redox peak, since for the lower Ni-to-Fe ratios, 2:1 and 4:1, the anodic peak is replaced by a shoulder-shaped peak. Trotochaud et al. [50] (and several references therein) have claimed that a positive potential shift of the redox peaks for Ni-Fe oxyhydroxide catalysts is associated with an increase in the OER activity. In general, it is well known that an addition of Fe to Ni-based oxides, hydroxides, and oxyhydroxides boosts the OER activity [50,80]. Our results agree with these findings (Fig. 1d). Here, the iR-corrected SV results show OER activity increase with an increase in the Fe content in the catalysts precursors. For the lowest used Fe content (Ni-to-Fe 16:1), the measured potential at  $10 \text{ mA cm}^{-2}$  is by ca. 100 mV lower than for the Ni-only sample. Further Fe addition results in an even higher OER activity, increasing the potential gap to the Ni-only case to ca. 130 mV at  $10 \text{ mA cm}^{-2}$ . Interestingly, no significant OER activity improvement happens anymore once the Ni-to-Fe ratio reaches 8:1. Here, it is worth noting that OER activity of a catalyst containing only Ni could be significantly increased by the presence of even trace Fe impurities in KOH used to prepare the electrolyte solutions [50]. In our work, the concentration of Fe impurities was much below the level necessary to impart an OER activity in the Ni-only reference catalyst that would be comparable to that of catalysts synthesized using both Ni and Fe precursors.

We also investigated the impact of an addition of a third metal on OER activity of the Ni-Fe aerogel-derived catalysts heat-treated at 150 °C. Two samples were synthesized containing Co or Mn, with the following atomic ratio of the three metals in the synthesis precursors: Ni-Fe-Co 8:1:1 and Ni-Fe-Mn 8:1:1. The results are shown in Fig. 1e–f, where the two ternary catalysts are compared with the NiFe8:1–150, the Ni-only catalysts, as well as with a commercial  $\text{IrO}_2$  catalyst. While the Ni(II)  $\rightleftharpoons$  Ni(III) CV redox peaks are still present in the ternary catalysts, the addition of Co and Mn does not improve the OER activity. In fact, the iR-corrected potentials measured at  $10 \text{ mA cm}^{-2}$  with the two catalysts are by ca. 50 mV higher than for the NiFe8:1–150 catalyst. Further investigations of the effect of a third transition metal are needed to better understand the interactions of these metals with the Ni-oxide matrix and their impact on the OER activity, including, for example, the exploration of other metals (e.g., Cu, Cr), different molar ratios, as well as a total replacement of Fe by other metals. It is also possible that catalysts containing different metals and/or in different molar ratios require a longer break-in for reaching their maximum OER activity. This study reveals that all the multi-metal aerogel-derived catalysts heat-treated at 150 °C are more OER-active than the Ni-only reference catalyst and the commercial  $\text{IrO}_2$  catalyst (a benchmark OER precious metal catalyst in acid media).

Finally, we also conducted a preliminary short-term durability test of the NiFe8:1–150 catalyst. We used SV to measure OER activity of the catalyst at the beginning of test (BOT), then held the current density at  $10 \text{ mA cm}^{-2}$  for 54 hours, and measured the OER activity again at the end of test (EOT). The results in Fig. 1g reveal an OER potential decrease by ca. 40 mV over the test duration, which corresponds to a degradation rate of  $0.74 \text{ mV h}^{-1}$ . As-recorded chronopotentiometric data in Fig. 1h attest to a degradation rate of  $0.83 \text{ mV h}^{-1}$  in a continuous (uninterrupted) experiment.

### 3.2. AEMWE testing

AEMWE testing involved two representative aerogel-derived catalysts: NiFe8:1–150 and NiFe8:1–500. They were derived from the same precursor (Ni-Fe aerogel with a Ni-to-Fe atomic ratio of 8:1) but heat-treated at different temperatures: 150 and 500 °C. In addition to their different electrochemical behavior in RDE testing and different OER activity, these two catalysts show substantial differences in terms of morphology, structure, and chemical composition (cf. characterization below). Fig. 2a shows polarization curves recorded with MEAs prepared in the same way but with the two different catalysts at the anode. For these tests, the catalysts were deposited onto a sintered platinumized Ti

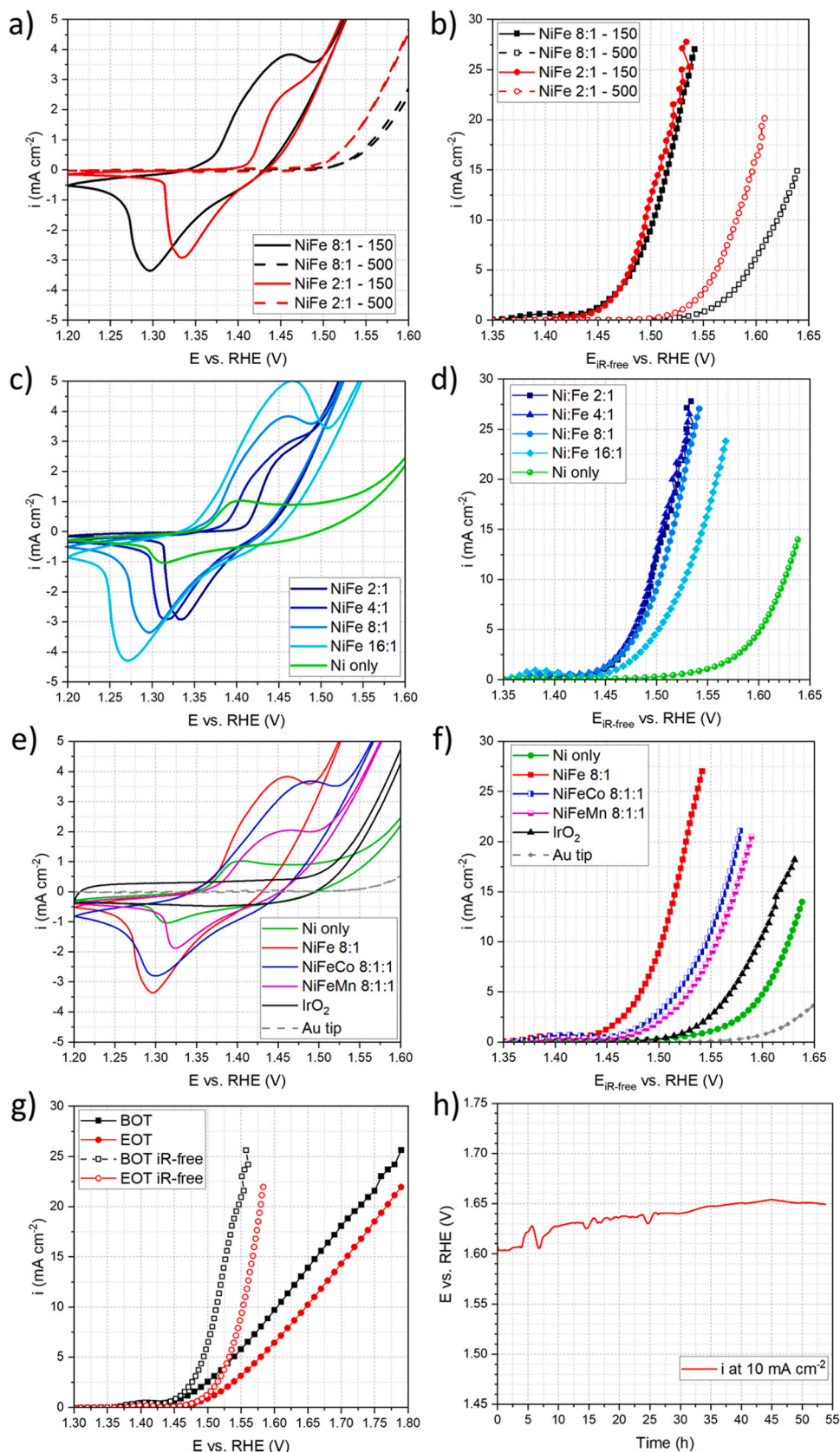


**Fig. 1.** a) CVs and b)  $iR$ -corrected SVs for catalysts derived from NiFe8:1 and NiFe2:1 aerogels after heat treatment at 150 and 500 °C. c) CVs and d)  $iR$ -corrected SVs for catalysts derived from aerogels with different Ni-to-Fe ratios heat-treated at 150 °C. e) CVs and f)  $iR$ -corrected SVs for catalysts derived from aerogels containing third transition metal (Co, Mn). Results for other catalysts are also shown for comparison. g) SVs with and without  $iR$  correction measured in for the NiFe8:1-150 catalyst before (BOT) and after (EOT) the 54-h stability test. h) Chronopotentiometry at 10 mA cm<sup>-2</sup> for NiFe8:1-150. All data were measured at RDE in N<sub>2</sub>-saturated 0.1 M KOH and at 1600 rpm. All CVs recorded at 10 mV s<sup>-1</sup> scan rate; all SVs recorded using 10 mV steps, and 10 s holds.

**Table 1**

BET surface areas and pore volumes for some of the aerogel-derived materials.

Catalyst	BET surface area ( $\text{m}^2 \text{g}^{-1}$ )	Pore volume ( $\text{cm}^3 \text{g}^{-1}$ )
Ni-150	425	1.29
NiFe8:1-150	382	0.85
NiFe8:1-500	55	0.21
NiFe2:1-150	552	0.97
NiFe2:1-500	64	0.34

foam PTL. Three AEMWE polarization curves were recorded with each MEA in DI water and two supporting electrolyte solutions, 1%  $\text{K}_2\text{CO}_3$  and 0.1 M KOH. The polarization curves in DI water reported here are after the MEA break-in, but before any measurements in supporting electrolytes. This latter aspect is especially important, as any residual contamination by supporting electrolyte must be avoided for pure-water measurements to be valid [27,30,81]. Regardless of the feed solution, the performance of the two catalysts reflects the OER activity trends measured in RDE, i.e., the catalyst heat-treated at 150 °C performs much better than the one heat-treated at 500 °C. The HFR values measured for the two MEAs during operation with different feeds are shown in Fig. 2b. The results confirm that the MEA HFR is not the reason for lower performance of the MEA having the NiFe8:1-500 catalyst at the anode. In fact, comparing the HFR values measured for the two MEAs in the same testing conditions, the MEA with the NiFe8:1-500 catalyst generally shows lower HFR, despite a much lower performance. Only in the DI-water case at current densities greater than  $0.7 \text{ A cm}^{-2}$  the HFR values for NiFe8:1-500 catalyst are higher than for the low-temperature catalyst, with a maximum difference of ca.  $0.1 \Omega \text{ cm}^2$ , which is still insufficient to justify the difference in the polarization curves. Consequently, the reason for the AEMWE performance difference are the anode catalysts themselves.

In 0.1 M KOH, when both the ionic conductivity and the OER kinetics are enhanced thanks to the large excess of  $\text{OH}^-$  ions, the difference in performance between the two MEAs is ca. 0.32 V (1.73 vs. 2.05 V) at  $1 \text{ A cm}^{-2}$ , and ca. 0.43 V at  $2 \text{ A cm}^{-2}$  (1.87 vs. 2.30 V). It must be noted that the anode catalyst layer (CL) fabrication process for these MEAs was not optimized for the catalyst loading or ionomer and binder content, which could have resulted in further increase the AEMWE performance. However, in our previous work, we demonstrated that these factors do not impact as much the performance when the AEMWE is operated with a supporting electrolyte feed as they do when the AEMWE is operated with DI water feed [30]. This is another evidence that the observed performance difference should be attributed to the anode catalyst activity. Similar results are obtained in 1%  $\text{K}_2\text{CO}_3$  feed. In general, better AEMWE performance is measured with KOH than with  $\text{K}_2\text{CO}_3$  electrolytes at a similar concentration primarily due to the higher pH and thus improved ionic conductivity in KOH. This is confirmed by the HFR results (Fig. 2b), with lower HFR measured in 0.1 M KOH than in 1%  $\text{K}_2\text{CO}_3$ . The HFR in 1%  $\text{K}_2\text{CO}_3$  is higher at low current densities and tends to decrease at high current densities, minimizing the HFR gap to 0.1 M KOH due to the so-called “self-purging effect”, allowing  $\text{CO}_3^{2-}$  ions to be removed from the membrane by the high flux of  $\text{OH}^-$  ions from the cathode to the anode [82].

The largest performance difference between the two catalysts was observed with DI water feed. The NiFe8:1-500 catalyst performed particularly badly in DI water, generating merely ca. 2.1 V at  $0.5 \text{ A cm}^{-2}$  and requiring as much as 0.3 V increase in the voltage to increase the current density by only  $0.1 \text{ A cm}^{-2}$ . The NiFe8:1-150 catalyst showed much better performance in DI water, superior even to that of the NiFe8:1-500 catalyst in supporting electrolyte. The voltage measured at  $1 \text{ A cm}^{-2}$  with NiFe8:1-150 catalyst in DI water was by ca. 0.2 V lower than that measured with NiFe8:1-500 catalyst in 0.1 M KOH. While even the initial electrolyzer performance of the NiFe8:1-500 catalyst is

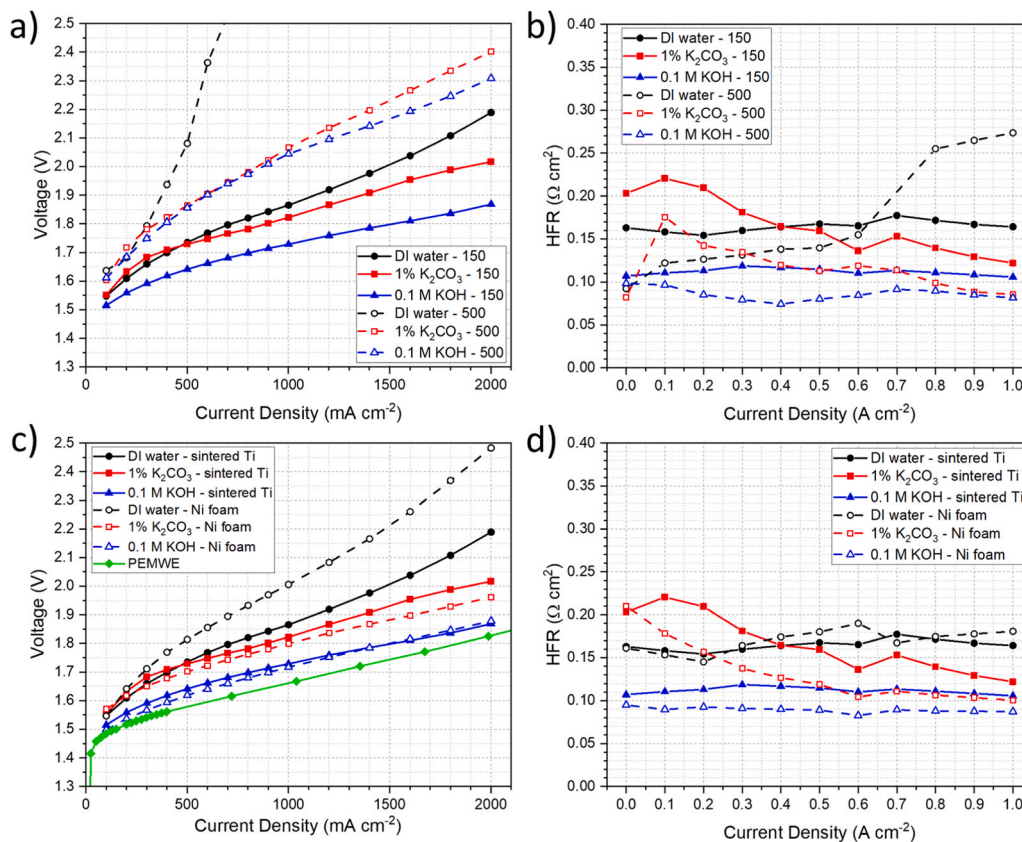


**Fig. 2.** a) Polarization curves and b) HFR values for NiFe8:1-150 and NiFe8:1-500 catalysts in the AEMWE anode. c) Polarization curves and d) HFR values for with NiFe8:1-150 catalyst deposited on two different PTL materials: Ni foam and sintered Ti.



inadequate for practical applications, that of the NiFe8:1–150 catalyst is promising. It is comparable with the best results reported to date, both in DI water and supporting electrolytes, as well as with both Ir-based and PGM-free catalysts [11,27,29,30,60,81–83].

To further validate our results, we compared the performance of the MEA prepared with the active NiFe8:1–150 catalyst at the anode with a similar MEA prepared using a commercial IrO<sub>2</sub> catalyst. The results are shown in Fig. S4. Overall, the IrO<sub>2</sub> catalyst showed better performance in 0.1 M KOH and 1% K<sub>2</sub>CO<sub>3</sub> supporting electrolytes than the PGM-free material, by ca. 0.1 V at 1 A cm<sup>-2</sup>, however, the NiFe8:1–150 catalyst performed better in DI water, by ca. 0.15 V at 1 A cm<sup>-2</sup>, which makes this catalyst even more promising for further studies.

We investigated the performance of the NiFe8:1–150 catalyst using two different PTL materials, a 275 μm thick platinized sintered Ti foam and a 290 μm thick Ni foam. A picture of the two PTL materials is shown in Fig. S2 (left). The sintered Ti foam appears less porous and smoother than the Ni foam. The AEMWE polarization curves recorded in DI water and two supporting electrolytes, and the respective HFR values are shown in Fig. 2c–d. The sintered Ti foam performs better in DI water compared to the Ni foam (by ca. 0.14 V at 1 A cm<sup>-2</sup>). The cell resistance is not the reason for this better performance, since HFR values for both MEAs are almost identical in DI water. A possible reason could be more effective interface between the CL and membrane, befitting from less porous and smoother surface of the sintered Ti foam, resulting in more uniform catalyst distribution during the catalyst ink spraying (ink not seeping into the PTL). The surface of the CLs deposited on sintered Ti foam and Ni foam is depicted in Fig S2 (center). Other possible reasons could be: (i) easier removal of O<sub>2</sub> bubbles; or (ii) formation of smaller bubbles due to the smaller pores in the Ti-foam PTL, favoring mass transport within the electrode. The impact of the PTL on the AEMWE performance has been investigated before and reported to be significant [84–86]. The Ni-foam PTL performs slightly better with supporting electrolytes, allowing for ca. 10 mV lower voltage in 0.1 M KOH below 1 A cm<sup>-2</sup>, and for a 10–50 mV lower voltage in 1% K<sub>2</sub>CO<sub>3</sub>. Possible reasons could be: (i) slightly lower HFR values (10–20 mΩ cm<sup>2</sup> in 0.1 M KOH, 30–50 mΩ cm<sup>2</sup> in 1% K<sub>2</sub>CO<sub>3</sub>) measured for the MEA with Ni foam PTL in presence of supporting electrolytes (Fig. 2d); and (ii) electrocatalytic contribution of Ni in the Ni-foam PTL.

A higher OER catalytic activity of catalysts deposited on the Ni foam compared to the platinized sintered Ti foam was measured in a three-electrode cell with 0.1 M KOH electrolyte in our previous work [30]. This catalytic contribution of the Ni foam can only be detected in the presence of a supporting electrolyte, where all the catalyst and PTL surfaces are entirely accessible by the OH<sup>-</sup> ions and therefore can contribute to the OER. This does not happen in the DI water operation of the AEMWE, where the conduction of the OH<sup>-</sup> ions from the AEM to the OER active sites only happens through the ionomer paths within the anode CL [87].

As mentioned before, the DI water polarization curves shown in Fig. 2a were measured after the cell break-in. To shed more light onto the activation of the MEAs prepared with the NiFe8:1–150 and the NiFe8:1–500 catalysts, several consecutive polarization curves in DI water at the beginning of test are shown in Fig. S7. A decrease in the voltage over time during three-minute current holds can be seen with both catalysts when recording the first polarization curve. A similar break-in behavior was reported previously for an MEA prepared using the same AEM and ionomer and a commercial IrO<sub>2</sub> anode catalyst [27]. However, the behavior of the NiFe8:1–150 catalyst (Figs. S7a–b) is substantially different compared to that of the NiFe8:1–500 catalyst (Figs. S7c–d). NiFe8:1–150 shows a continuous decrease in the voltage during up to ten consecutive polarization curves. Voltage stabilization at high current densities takes longer time, i.e., a higher number of polarization curves, while at low current densities, 0.1 and 0.2 A cm<sup>-2</sup>, the voltage stabilization occurs already after the first or second polarization curve. The NiFe8:1–500 catalyst shows a slight voltage decrease at low current densities (up to 0.5 A cm<sup>-2</sup>) during the fifth consecutive

polarization curves. However, at high current densities, the performance starts to decrease already during the second polarization curve. Since an excessively high voltage of 2.78 V at 1 A cm<sup>-2</sup> was reached with this catalyst already after the fifth polarization curves, we decided to stop the MEA break-in process at this point.

The durability of the NiFe8:1–150 catalyst was assessed in 1 M KOH supporting electrolyte, to avoid the complicating factors of CL delamination, ionomer degradation, and the loss of ionic conductivity within the catalyst layer, which were reported to heavily affect the AEMWE durability in DI water [30,88,89]. The results are shown in Fig. 3. First, a 175-mV improvement in voltage at 1 A cm<sup>-2</sup> with the NiFe8:1–150 catalyst was obtained compared to the commercial NiFe<sub>2</sub>O<sub>4</sub> catalyst (Fig. 3a). The NiFe8:1–150 MEA was then tested for durability during a 110-hour galvanostatic hold at 1 A cm<sup>-2</sup> (Fig. 3b). The voltage required to maintain the latter current density increased relatively quickly at the beginning of the test, but the rate of loss decreased over time. The overall degradation rate was 0.49 mV h<sup>-1</sup>, while the degradation rate over the final 10 h of the measurement was only 0.05 mV h<sup>-1</sup>. Interestingly, the polarization curve after 110 hours demonstrates an increase in the voltage at 1 A cm<sup>-2</sup> (1.665 vs. 1.643 V), but of a smaller magnitude than the loss observed in the steady state measurement.

To compare our AEMWE performance results recorded in different electrolytes, 0.1 M KOH, 1.0 M KOH, and pure water feed, with the results published by other groups, we used current density values measured at 1.8 V and 2.0 V. Our current density at 1.8 V in DI water, ca. 0.7 A cm<sup>-2</sup>, approached the highest value previously reported [60]. In 0.1 M KOH, our result of ca. 1.5 A cm<sup>-2</sup> at 1.8 V is among the best reported to date [90]. In 1.0 M KOH, our values of ca. 2.5 and ca. 3.75 A cm<sup>-2</sup> measured at 1.8 and 2.0 V, respectively, also rank close to the best reported results [60,90,91]. When comparing such performance values, one should remember though that they often depend on other factors than OER activity itself, such as the membrane, catalyst loading, ionomer and its amount, type of the porous transport layer, electrode and MEA fabrication methods, cathode electrocatalyst, supporting electrolyte and its concentration, as well as the test conditions (temperature, pressure, flow rates), etc.

### 3.3. Physical and chemical characterization of catalysts before testing

#### 3.3.1. N<sub>2</sub> physisorption

We measured the BET surface area and pore-size distribution of five representative aerogel-derived catalyst samples, obtained from precursors with three different chemical compositions: one with only Ni, one with a higher Ni-to-Fe atomic ratio (8:1), and one with a lower Ni-to-Fe atomic ratio (2:1). Of the samples containing Fe, one was heat-treated at 150 °C and one heat-treated at 500 °C. The results are reported in Table 1. The adsorption and desorption isotherms and DFT pore-size distribution plots for the same samples are shown in Fig. 4a–b. The samples heat-treated at 150 °C reach surface areas of several hundreds of m<sup>2</sup> g<sup>-1</sup>, confirming the effectiveness of the supercritical CO<sub>2</sub> drying method in generating aerogels with large surface, as also reported in previous works [48,59,92]. The samples heat-treated at 500 °C have 7–8 times lower surface area, and 3–4 times lower pore volume, confirmed by the lower volumes of adsorbed N<sub>2</sub> in the adsorption and desorption isotherms at all the relative pressure values (Fig. 4a). Most of the pores in the aerogels heat-treated at 150 °C have a diameter between 1 and 10 nm, and ultra-small micropores between 0.5 and 0.8 nm are also present. The NiFe2:1–150 sample shows a particularly high amount of mesopores between 3 and 6 nm, which are likely associated with the slight hysteresis loop observed in the adsorption-desorption isotherms for this sample. This hysteresis has been reported to be associated with non-rigid aggregates of plate-like particles [93]. In addition to causing a massive surface area decrease (associated with a substantial structural reconfiguration, see below), the heat treatment at 500 °C results in much lower micropore and mesopore content, with pores larger than 10 nm dominating.



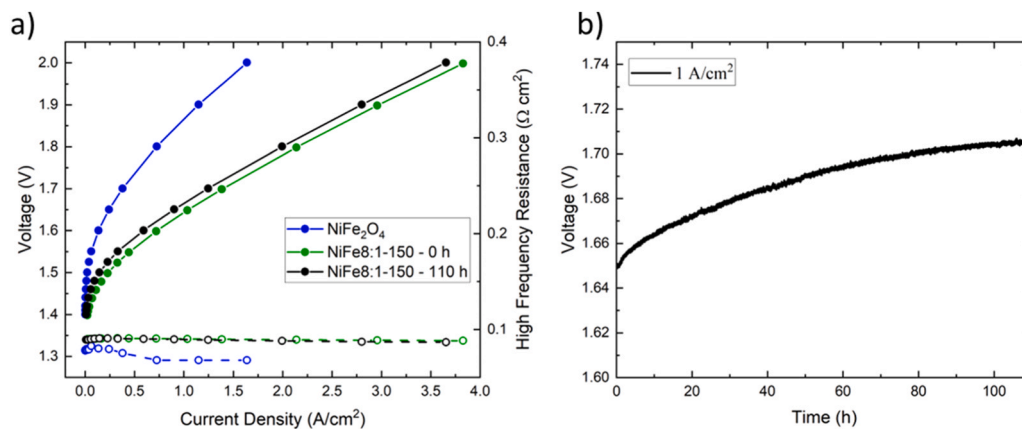


**Fig. 3.** Durability test of NiFe8:1-150 catalyst. a) Polarization curve and HFR values for a commercial NiFe<sub>2</sub>O<sub>4</sub> anode and the NiFe8:1-150 anode before and after the 110-h durability test. b) Durability test at 1 A cm<sup>-2</sup> as voltage vs. time plot. The measurements were done with an AEMWE fed with 1 M KOH at 80 °C, a Pt/C cathode, and a Ni fiber PTL.

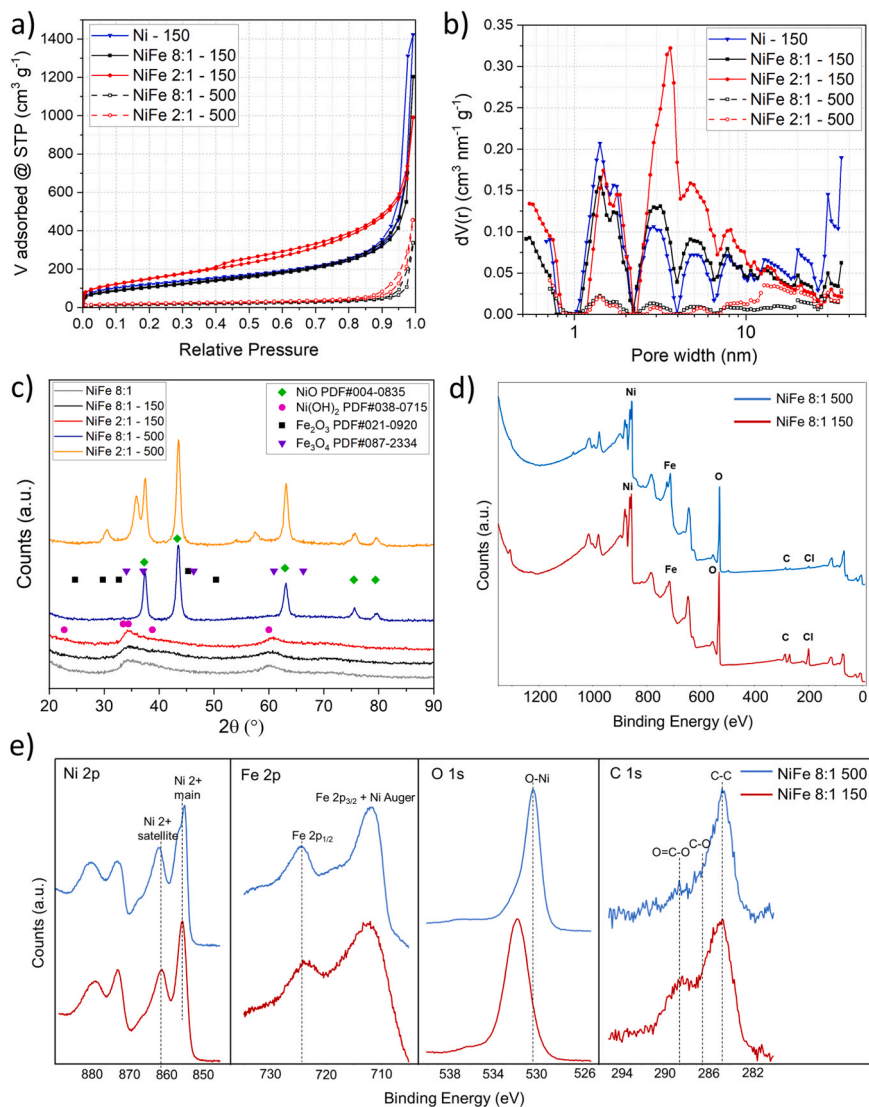


**Fig. 4.** a) N<sub>2</sub> adsorption/desorption isotherms, b) differential pore size distribution, and c) XRD spectra of some of the Ni-Fe aerogel-derived catalysts. d) XPS survey spectra and e) XPS high resolution peaks related to the Ni, Fe, O and C elements for the NiFe8:1-150 and the NiFe8:1-500 catalysts.

### 3.3.2. XRD

The XRD spectra of representative aerogel samples are shown in Fig. 4c, with those of the as-prepared NiFe 8:1 catalysts and after its heat treatment at 150 °C being practically identical (gray and black lines in Fig. 4c), an indication that the heat treatment at this relatively low temperature results in the removal of the physisorbed water without a structural change. On the other hand, heat treatment at 500 °C causes a substantial change in the structure of the NiFe 8:1 (blue line in Fig. 4c). To understand the possible effect of the Ni-to-Fe ratio we also recorded an XRD spectrum for the NiFe 2:1 sample heat-treated at 150 °C (red line in Fig. 4c), which looks identical to those obtained with NiFe 8:1. No characteristic peaks can be attributed to particular crystalline structures, which is typical for amorphous materials. Similar results were reported for other Ni-, Ni-Fe-, Cu-, and Co-oxide aerogels [48,59,69,92]. Another possible reason could be that the Ni, Fe, or Ni-Fe oxide/hydroxide particles in these materials, while still crystalline, are too small to give rise to a characteristic detectable X-ray diffraction signal (cf., the discussion of high-resolution STEM results below). The presence of two low-intensity and very broad peaks at  $2\theta$  angle of ca. 60° and ca. 33° could be also tentatively assigned to Ni hydroxide  $\text{Ni(OH)}_2 \cdot 0.75 \text{H}_2\text{O}$ , PDF # 038–0715). After the heat treatment at 500 °C, the NiFe 8:1 sample shows sharp and well-defined XRD peaks corresponding to the NiO structure (PDF # 004–0835), implying a much larger crystallite size. The formation of large crystals by agglomeration/sintering is likely induced by the heat treatment at high temperature [94,95]. No peaks corresponding to Fe-containing oxides are present, indicating that Fe atoms are incorporated into the NiO structure by substituting Ni atoms. In addition to peaks due to NiO, the NiFe 2:1 sample heat-treated at 500 °C shows additional peaks at  $2\theta$  angles ca. 31, 36, 54, and 57°. Although this XRD pattern has not been found to correspond uniquely to a specific crystalline structure, the additional peaks can be tentatively attributed to Fe-containing oxides such as for example  $\text{Fe}_3\text{O}_4$  (PDF # 087–2334) or  $\text{Fe}_2\text{O}_3$  (PDF # 021–0920), which are likely formed due to the high Fe content in this sample.

### 3.3.3. XPS

The near-surface elemental composition of two reference materials, NiFe8:1–150 and NiFe8:1–500, is shown in Fig. 4d, while the atomic % content of each detected element is shown in Table 2. As expected, Ni, Fe, and O are detected in both materials. C and Cl likely originate from the synthesis precursors: Cl in Ni and Fe chlorides, and C in the PAA nucleation agent. The much lower level of both C and Cl detected in NiFe8:1–500 than in NiFe8:1–150 is likely due to a difference in heat-treatment temperatures in air. The quantitative analysis reveals that the Ni-to-Fe atomic ratio near the NiFe8:1–150 catalyst surface is almost double that expected based on the initial ratio in the precursors (15.7 vs. 8), while it is lower (6.2 vs. 8) for the NiFe8:1–500, indicating opposite distribution trends for these elements from the surface to the bulk in these two catalysts. The (Ni+Fe)-to-O atomic ratio for these two catalysts is also different, being lower for NiFe8:1–150 (0.58 vs. 0.80), which is consistent with EDS analysis (see below), and in agreement with the presence of Ni hydroxide on the surface of NiFe8:1–150.

The high resolution Ni spectrum of NiFe8:1–150 in Fig. 4e reveals the presence of a 2p 3/2 peak at 855.3 eV and 2p 1/2 peak at 873.1 eV, with a gap of 17.8 eV. For NiFe8:1–500, the same peaks are at 854.8 eV and 872.9 eV, with a gap of 18.1 eV. The Ni spectrum of NiFe8:1–500 is

**Table 2**

Near-surface elemental composition in atomic % measured by XPS for the NiFe8:1 catalyst heat-treated at 150 °C and 500 °C.

Catalyst	Ni (at %)	Fe (at %)	O (at %)	C (at %)	Cl (at %)	Ni-to- Fe ratio	(Ni+Fe):O ratio
NiFe8:1–150	26.7	1.7	49.0	13.8	8.8	15.7	0.58
NiFe8:1–500	36.2	5.8	52.4	4.4	1.2	6.2	0.80

very close to the reference spectrum of NiO in terms of the peak shape (the presence of a shoulder in the 2p 3/2 Ni peak) and gap between the 2p 3/2 and the 2p 1/2 peaks, as reported for a standard material [96].

The shape of the Ni 2p 3/2 peak for the NiFe8:1–150 catalyst, which does not have a shoulder, is similar to that of  $\text{Ni(OH)}_2$  [97]. Therefore, the surface of this catalyst may contain  $\text{Ni(OH)}_2$ , as also suggested by the BE values of the O spectra (Fig. 4e): 531.7 eV for NiFe8:1–150 which is close to the values reported for  $\text{Ni(OH)}_2$  and  $\text{Ni}_2\text{O}_3$ , and 530.2 eV for NiFe8:1–500 which points to NiO [96]. These results are also in agreement with the higher (Ni+Fe)-to-O atomic ratio for NiFe8:1–150 compared to NiFe8:1–500.

No noticeable difference was detected in the Fe spectra for the two catalysts. The lower Ni-to-Fe ratio for NiFe8:1–500 confirms the near-surface enrichment for this catalyst in Fe, as found in the EDS mapping (see below in Section 3.3.4).

### 3.3.4. STEM-EDS-EELS

Scanning transmission electron microscopy was used to further elucidate the microstructure of the aerogel catalyst. Fig. 5 shows the SE and HAADF images of the NiFe 8:1 aerogel before and after heat treatment at 150 °C (Fig. 5a–b and Fig. 5c–d, respectively), and after heat treatment at 500 °C (Fig. 5e–f). No major differences in the morphology before and after heat treatment at 150 °C is in agreement with XRD results, showing that no structural modification occurs at this temperature. Both materials have a fluffy and spongy morphology with a high level of porosity, as expected from an aerogel-like structure with high surface area and pore volume. The sample heat-treated at 500 °C shows the presence of crystallites with a size of 10–20 nm, connected to form larger agglomerates, again, confirming the XRD result that substantial structural modification is caused by the higher of the heat-treatment temperatures. The bulk elemental composition of these materials was determined by EDS (first three rows in Table 3). All the materials show a Ni-to-Fe atomic ratio very close to the nominal value of 8:1 in the synthesis precursors. The non-heat-treated aerogel and NiFe8:1–150 have very similar elemental composition, suggesting that the heat treatment at 150 °C does not alter the chemical composition of the original aerogel. The (Ni+Fe)-to-O ratio in NiFe8:1–500 is higher than in NiFe8:1–150, confirming the XPS results in Table 2. Figs. S8a–b show low-resolution STEM images with EDS mapping for NiFe8:1–150 and NiFe8:1–500 highlighting a homogeneous distribution of Ni, Fe, and O at a larger scale.

Further insights into the catalyst morphology, structure, and chemical composition are provided by the high-resolution STEM images and corresponding EDS maps in Fig. 6. Even at a high resolution (Fig. 6a), the structure of the NiFe8:1–150 catalyst appears disordered and the Fe distribution within the Ni matrix random. The atomic resolution image for this catalyst (Fig. 6c) reveals the presence of small crystallite domains with only a handful of atomic layers aligned in ordered structures, 1–2 nm in size, randomly oriented, in agreement with the lack of well-defined diffraction peaks in the XRD spectra. As already evident from the lower resolution images, the NiFe8:1–500 catalyst (Fig. 6b) reveals the presence of much larger crystallites, 10–20 nm size. The high-resolution EDS mapping attests to preferential distribution of Fe atoms near the surface of the nanoparticles, confirming the XPS results, which unveiled lower than nominal Ni-to-Fe ratio in the catalyst. The Fe segregation to the surface of crystals was also observed by Abbott et al. [55] for Ni-Fe oxide materials with Ni-to-Fe ratios of 9:1 and 7:3, similar to that used in this work. The atomic resolution image in Fig. 6d shows that an individual crystallite of ca. 15 nm is composed of several tens of orderly aligned atom layers.

Fig. 6e shows EELS spectra of the O K-edge signal acquired on two different areas for both the NiFe8:1–150 and the NiFe8:1–500 catalysts. Bulk NiO typically exhibits six main features in the O K-edge spectrum [98], labeled as A–F in Fig. 6e. Peak A corresponds to the transition from O 1s electron to antibonding O 2p states hybridized with 3d Ni states which are localized around Ni atoms. This feature is present in both

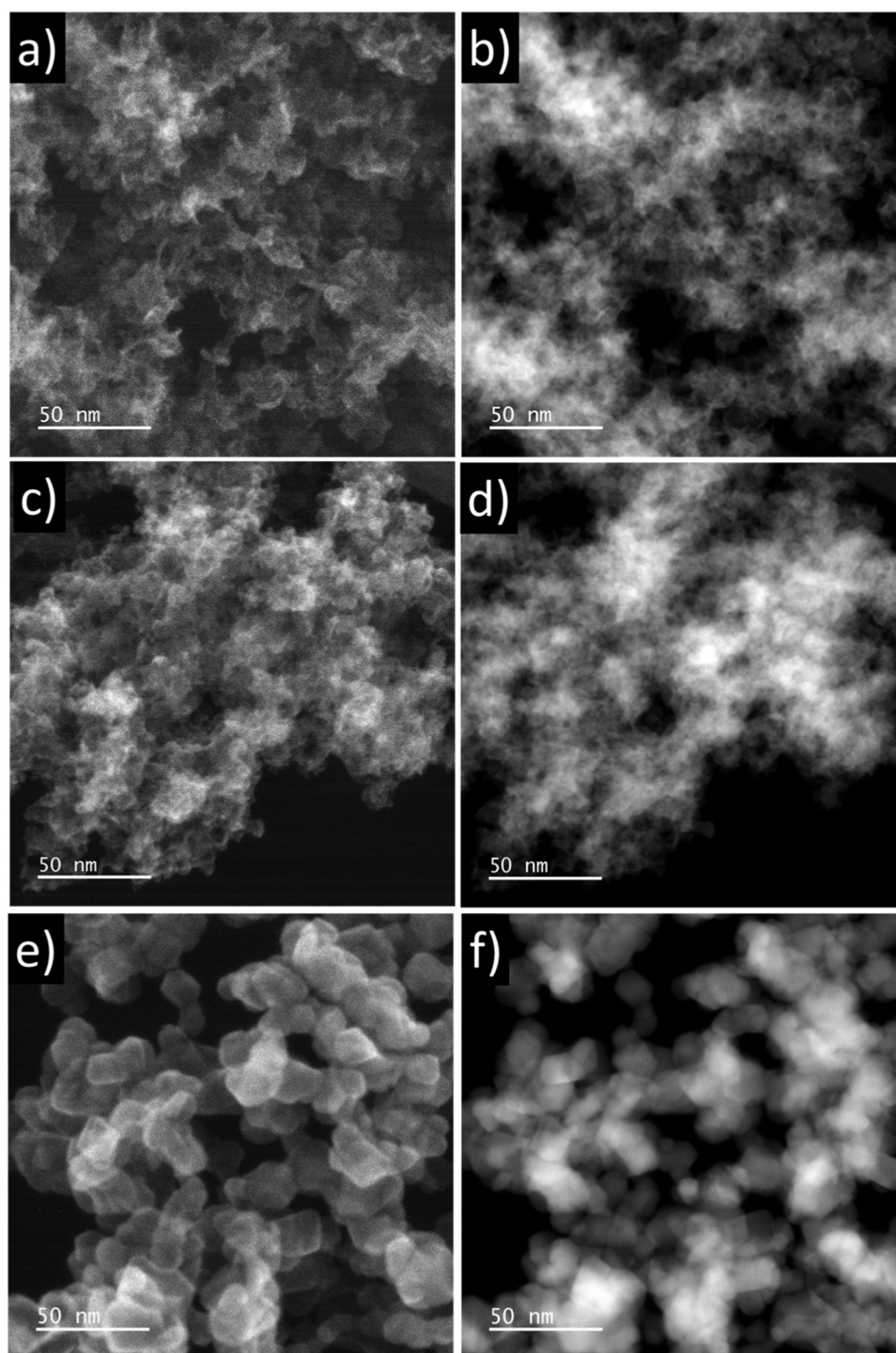


**Fig. 5.** a) SE- and b) HAADF-STEM images of Ni-Fe 8:1 aerogel. c) SE- and d) HAADF-STEM images of NiFe8:1-150 catalyst. e) SE-STEM and f) HAADF-STEM images of NiFe8:1-500 catalyst.

NiFe8:1-150 and NiFe8:1-500. Peaks **B**, **D**, and **E** involve multiple scattering (MS) arising from medium- and long-range contributions. Peak **C** is associated with MS within the first O shell, and peak **F** is associated with the single scattering (SS) from the nearest neighbor O shell. Materials characterized by a higher degree of disorder should exhibit only contributions from short-range SS and MS, lacking contributions from medium- and long-range order [98]. An increase in disorder at large distances should thus lead to less pronounced or missing features of **B**, **D**, and **E** peaks. Our samples exhibit a similar change of disorder in the O K-edge spectrum with 150 °C and 500 °C

heat-treatment temperatures. NiFe8:1-500 shows clear features for the **A**, **B**, **C**, **D**, and **F** peaks, while NiFe8:1-150 shows only **A**, **C**, and **F** peaks, suggesting a highly disordered structure for this catalyst. This is in full agreement with the micrographs and EDS maps in Fig. 6a-d where the NiFe8:1-150 shows small randomly oriented crystallites. On the other hand, NiFe8:1-500 shows larger crystallites (10–20 nm), but still with certain level of disorder, since a pronounced **E** peak is still missing compared to the spectrum of bulk NiO reported in the literature [98].



**Table 3**

Elemental composition in atomic % measured by EDS for the Ni-Fe 8:1 catalyst before and after the heat treatment at 150 °C and 500 °C, and for the heat-treated catalysts after testing in AEMWE (in this case the catalysts were mixed with ionomer).

Catalyst	O (at %)	Fe (at %)	Ni (at %)	Ni-to-Fe ratio	(Ni+Fe)-to-O ratio
NiFe8:1aerogel	75.5 ± 0.5	3.0 ± 0.1	21.5 ± 0.5	7.2	0.33
NiFe8:1-150 before test	74.1 ± 0.5	3.1 ± 0.05	22.8 ± 0.5	7.4	0.34
NiFe8:1-500 before test	68.0 ± 0.2	3.8 ± 0.03	28.2 ± 0.2	7.3	0.47
NiFe8:1-150 after test	79.7 ± 1.2	2.6 ± 0.45	17.7 ± 1.0	6.9	0.27
NiFe8:1-500 after test	66.6 ± 1.2	3.5 ± 0.4	30.0 ± 1.0	8.7	0.50

### 3.3.5. XAS

As evident in the Fourier transform of the Ni K edge extended X-ray absorption fine structure (EXAFS) data and the edge energy of the X-ray absorption near edge spectra (XANES) in Fig. 7, the Ni in the as-prepared NiFe8:1 catalyst powder prior to heat treatment and after heat treatment at 150 °C, has a coordination environment and oxidation state similar to that of the Ni(OH)<sub>2</sub> standard (Fig. 7a-c), consistent with the XPS and XRD data. Slight differences in the intensity of the second shell scattering at 2.77 Å are observed between the catalyst samples and the standard which can be attributed to disorder in the atomic structure of the catalyst, in agreement with observations in Fig. 6c where crystalline domains are small and disordered. As shown in Fig. 7b-d, after heat treatment of the powder at 500 °C, the Ni K-edge spectrum is nearly identical to that of the NiO standard, also consistent with the XPS and XRD data. The Ni coordination environment and oxidation state are subtly changed by incorporation and testing in an AEMWE for both the NiFe8:1-150 and NiFe8:1-500 catalysts. As shown in Fig. 7 and in the inverse Fourier transform of Fig. S9, the second shell scattering of Ni in the NiFe8:1-150 catalyst is altered by testing in the MEA with the

changes consistent with either a decrease in the second shell coordination number or interference between the first and second shell scattering paths indicative of alteration of the long-range order of the catalyst by testing in the MEA. Testing of the Ni-to-Fe8:1-500 catalyst in an MEA has less of an impact on the Ni structure than for the NiFe8:1-150 catalyst with slight decrease of intensity of the second shell scattering indicative of a slight decrease in the second shell coordination number.

As shown in the Fourier transform of the Fe K-edge spectra (Fig. 8a), Fe in the as-prepared Ni-Fe8:1 powder, prior to heat treatment and after heat treatment at 150 °C has a first shell Fe-O peak position similar to that of the  $\gamma$ -Fe(OH)<sub>3</sub> standard and a second shell peak position similar to that of the  $\alpha$ -Ni(OH)<sub>2</sub> standard. This is indicative of Fe incorporation into the  $\alpha$ -Ni(OH)<sub>2</sub> structure. The energy of the absorption edge for these materials indicates that Fe is in the 3+ oxidation state. After heat treatment at 500 °C, the Fe coordination environment is like that of the Fe<sub>3</sub>O<sub>4</sub> standard, as shown in the Fourier transform of the EXAFS data in Fig. 8b, consistent with the EDS data (Fig. 6b) showing Fe segregation to the surface of the predominantly NiO particle core forming a separate Fe<sub>3</sub>O<sub>4</sub> phase. The lower edge energy and lower “white line” intensity for the NiFe8:1-500 catalyst as compared to that of the NiFe8:1-150 catalyst are consistent with a lower average oxidation state of Fe in this material (i.e., 2.67+ for Fe<sub>3</sub>O<sub>4</sub> vs. 3+ for Fe(OH)<sub>3</sub>). The Fe spectra for both NiFe8:1-150 and NiFe8:1-500 are nearly unchanged by testing in an AEMWE, with the NiFe8:1-500 catalyst showing slight increases in scattering intensity indicative of particle growth.

### 3.3.6. Mössbauer spectroscopy

The spectrum measured at a room temperature with the as-prepared fresh NiFe8:1-150 did not show any measurable signal, despite 7 days of acquisition time. This indicates an overly soft lattice, as could be expected of an aerogel. A spectrum was observed upon cooling to 50 K, revealing an Fe(III) doublet spectrum. Subsequent systematic measurements of the temperature dependence were carried out three months after synthesis on samples exposed to ambient atmosphere. Though the spectrum at 50 K showed identical spectral parameters compared to that measured initially, much stronger absorption was observed, enabling a

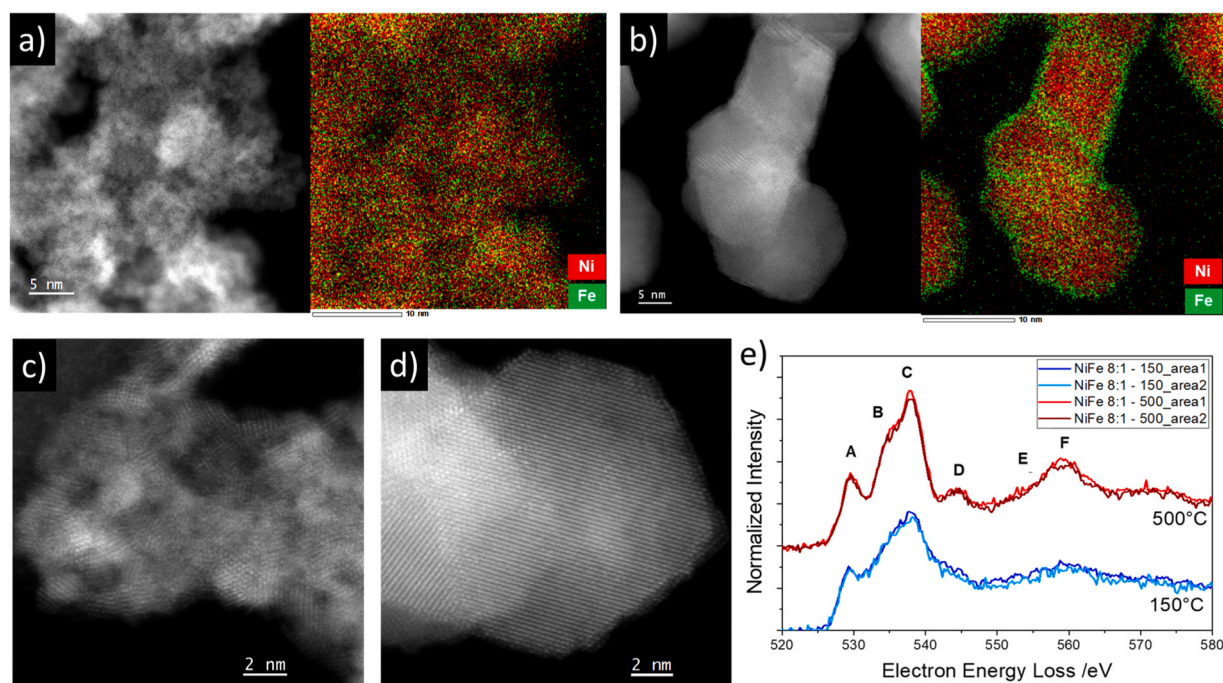


**Fig. 6.** a) High resolution HAADF-STEM image with Ni and Fe elements EDS mapping of NiFe8:1-150. b) High resolution HAADF-STEM image with Ni and Fe elements EDS mapping of NiFe8:1-500. c) Atomic-resolution HAADF-STEM image of the NiFe8:1-150 catalyst. d) Atomic-resolution HAADF-STEM image of NiFe8:1-500. e) EELS of O K-edge on two different areas of NiFe8:1-150 and NiFe8:1-500.



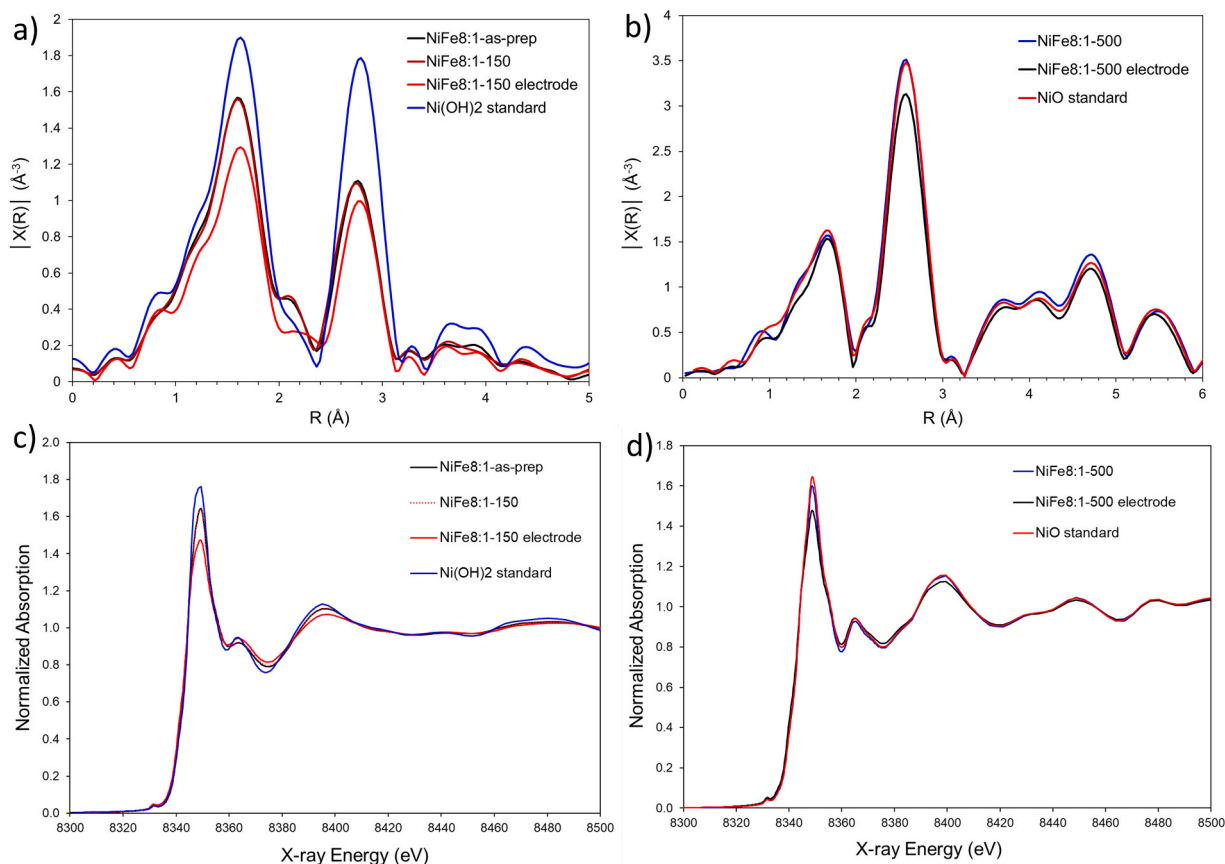


**Fig. 7.** a-b) Fourier transforms of the Ni K-edge EXAFS and c-d) XANES data for the NiFe8:1 catalyst as-prepared, after heat treatment at 150 °C (a-c), after heat treatment at 500 °C b-d), and for the latter two materials after testing in the anode of an AEMWE. Fourier transforms and XANES data for Ni(OH)<sub>2</sub> and NiO standards are also shown for comparison.

temperature-dependent study between 6.5 and 260 K. The onset of magnetic hyperfine splitting was observed below 30 K. At 6.5 K, a sextet spectrum with rather broad distribution of hyperfine fields was observed. (Fig. 9a). The weak absorption prevented the acquisition of data with high signal to noise over reasonable counting times. Hence, only a phenomenological fit model with four sextets was used which provided the maximum and average hyperfine fields of  $\mu_0 H_{\max} = 50.4$  T and  $\mu_0 H_{\text{av}} = 38.6$  T, respectively. The average isomer shift and quadrupole splitting were  $0.43 \text{ mm s}^{-1}$  and  $0.27 \text{ mm s}^{-1}$ , respectively. Combined, these parameters indicate high-spin Fe(III) as a majority Fe state. Many Fe and Ni oxides and hydroxides order magnetically above room temperature, hence the low onset temperature for magnetic splitting indicates either nanosized particles and superparamagnetic behavior or a specific species with low ordering temperature. The maximal hyperfine field suggest  $\alpha\text{-FeOOH}$  as the closest match in common species. The spectrum in Fig. 9a and the ordering temperature resembles that observed by Hunter et al. [99] on a polarized sample, but exhibits much sharper edges at high-velocity, indicating a more narrow hyperfine field distribution. The isomer shift and hyperfine splitting of the 6.5 K spectrum also exclude Fe(II) in  $\text{Fe(OH)}_2$  form as majority species, which exhibits a four-line spectrum at positions incompatible with our observation [100].

Upon heating from 30 to 260 K, doublet spectra (similar to that at 295 K but with poorer statistics) were observed with parameters as shown in Fig. 9b, confirming Fe(III) as the majority species. Analysis of the spectral area above 50 K with a Debye model for the Lamb-Mössbauer factor indicates a very soft lattice, with a  $153(10)$  K Debye temperature. The decrease in spectral area (Fig. 9c) is probing the acoustic range of the phonon spectrum. Below 50 K, a rapid increase in area is observed. This could indicate either magnetoelastic coupling or

that part of the area is lost due to broad superparamagnetic relaxation. Only a future study with isotopically enriched samples can clarify this. The quadrupole splitting,  $\Delta E_Q$ , is constant at  $0.6 \text{ mm s}^{-1}$  (Fig. 9d), slightly larger than in the magnetic phase, indicating a possible canting between the principal axis of the electric field gradient and the hyperfine field. The isomer shift,  $\delta$ , shows the typical small decrease as a function of temperature corresponding to the second-order Doppler shift (SOD), with a characteristic  $\Theta_D$  of  $\sim 600(50)$  K (see Fig. 9d). Note that the SOD is probing the kinetic energy of the Fe ions, which is heavily weighted towards optical phonons.

Six months after synthesis, we measured an additional spectrum at room temperature in a narrower velocity range (Fig. 9b), to obtain better statistics. Due to different geometries of the spectrometer for the two measurements, the spectral area cannot be directly compared with that in Fig. 9c. This spectrum was fit with two narrow Fe(III) doublets,  $\Gamma \sim 0.26 \text{ mm s}^{-1}$  linewidth, with  $\delta \sim 0.34(1) \text{ mm s}^{-1}$  and  $\sim 0.40(3) \text{ mm s}^{-1}$ , and  $\Delta E_Q \sim 0.46(1)$  and  $0.70(10) \text{ mm s}^{-1}$ , for 79 and 15% of the spectral area, respectively. The former doublet has parameters very close to those of superparamagnetic  $\alpha\text{-FeOOH}$  goethite ( $\delta = 0.33 \text{ mm s}^{-1}$  and  $\Delta E_Q = 0.5 \text{ mm s}^{-1}$  at 351 K) [101]. A remaining spectral component, 6% area, at low velocity could be fit only with a narrow doublet,  $\Gamma \sim 0.27 \text{ mm s}^{-1}$ , with  $-0.06(5) \text{ mm s}^{-1}$  isomer shift, and  $0.2(1) \text{ mm s}^{-1}$  quadrupole splitting. These parameters are rather surprising, as they suggest a small fraction of tetravalent Fe. These parameters are similar to those found for a minority Fe(IV) component by Axmann and Glemser [102] on a discharged sample and by Hunter et al. [99] on polarized samples. Surprisingly, this small Fe(IV) component is stable at ambient condition in material that was not subjected to any potential cycling. In addition, the initial spectrum at 200 K (see Fig. S10), did not show the asymmetry in the spectrum associated with this Fe(IV) component. DFT

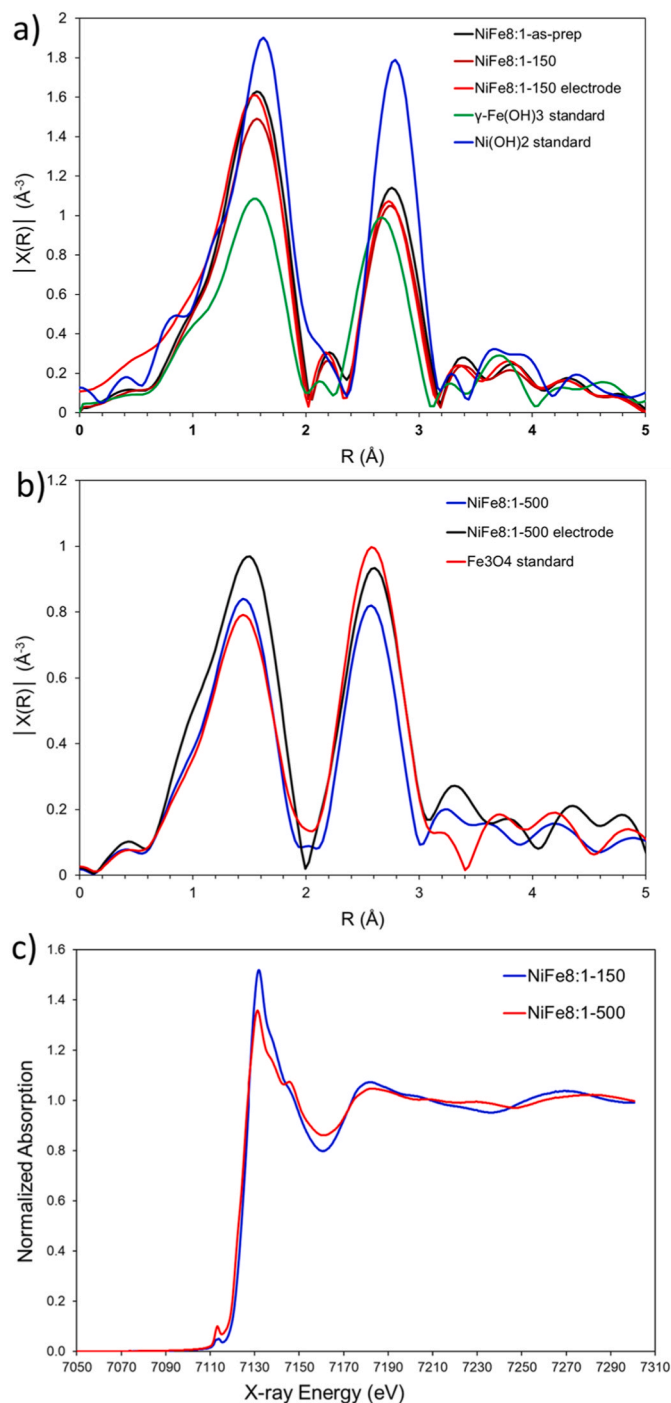


**Fig. 8.** a-b) Fourier transforms of the Fe K-edge EXAFS and c) XANES data for as-prepared NiFe8:1 and after heat treatment at 150 °C (a), after heat treatment at 500 °C (b), and for the latter two material after testing in the AEMWE. Fourier transforms for  $\gamma\text{-Fe}(\text{OH})_3$ ,  $\text{Ni}(\text{OH})_2$ , and  $\text{Fe}_3\text{O}_4$  standards are also shown for comparison.

atomistic modeling predicted the presence of Fe(IV) in highly OER-active Ni-Fe catalysts [103]. Other important information that can be deduced from this spectrum is that the local environment of Fe is not  $\text{NiO}$ , which was reported to exhibit a single line trivalent iron spectrum with  $\delta \sim 0.4 \text{ mm s}^{-1}$  [104]. Overall, the spectral parameters observed here agree with earlier work [102], that indicates that these aerogel-derived Ni-Fe catalysts do not feature  $\text{FeOOH}$  in  $\text{Ni}(\text{OH})_2$  but rather an intimate atomic scale mixing, in agreement with microscopy observations in Fig. 6a and Fig. S15, in which Fe retains most

characteristics of  $\alpha\text{-FeOOH}$ . Combining the information of the spectral parameters and their evolution over time, we can report that there is very little change in the local Fe chemistry, as all the spectra exhibit the characteristic doublet shape observed at 295 K, with small changes in the asymmetry of the spectrum (see Fig. S10), which we can only attribute to ageing (shelf-life). However, we suspect a quite dramatic evolution of the material microstructure because we observe a significant increase in spectral area over time. The most likely reason for this increase is grain coarsening and possibly also migration of Fe within grains from surface to interior of particles, both of which would lead to an increase in the Lamb-Mössbauer factor.

The Mössbauer spectral analysis of the NiFe8:1–500 catalysts reveals a quite different behavior. The spectra at 6.5 and 295 K (see Fig. S11), are characteristic for typical magnetic iron oxides ( $\delta = 0.42(1)$  and  $0.38(1) \text{ mm s}^{-1}$ , respectively), albeit with a broad distribution of hyperfine fields of  $\mu_0 H_{\text{av}} \sim 50 \text{ T}$  at 6.5 K. Confirmation that particles are larger than in the NiFe8:1–150 sample, is the fact that hyperfine splitting persists at room temperature, and only  $\sim 6\%$  of area corresponds to a field of  $\mu_0 H_{\text{av}} \sim 26 \text{ T}$  and 4% is paramagnetic. The lattice is more rigid, with 240 K Debye temperature estimate from the area at 6.5 and 295 K.

### 3.4. Physical and chemical characterization of catalysts after test

After completing the test of the MEAs prepared with the NiFe8:1–150 catalyst and two different PTLs (sintered Ti foam and Ni foam), we opened the electrolyzer cell and observed the electrodes. The pictures of the two electrodes after testing are shown in Figs. S2a–b (right side). The color of the catalyst changed completely to black compared to the yellow-green color of the electrodes before testing (Figs. S2a–b, center), which is the same as the color of the original catalyst powder (Fig. S1b). We visually inspected the electrode prepared by depositing NiFe8:1–500 onto sintered Ti foam PTL after testing (Fig. S3). In this case, we did not observe a substantial color change compared to the beginning of test, with the electrode still having the same dark brown color of the original catalyst powder before testing (see Fig. S1b). The observation of the change in color for the NiFe8:1–150 catalyst after testing, but not for the NiFe8:1–500, together with their different performance and activation behaviors, prompted further characterizations of the two catalysts after testing.

The comparison of NiFe8:1–150 before (Fig. 5c–d and Fig. 6a–c) and after (Fig. 10a and Fig. S12a–b–c) reveals a substantial change in morphology from porous/spongy to platelet-needle-like, indicating that the original catalyst undergoes a phase transformation during the electrolyzer anode operation. This electrochemically-induced phase change is characteristic for  $\text{Ni}(\text{OH})_2$ -based materials, in which the layered structure undergoes rotation, translation, and intercalation of ions/electrolyte when subjected to dynamic electrode potentials [46]. Such changes are not observed in the NiFe8:1–500 catalyst, which shows no morphology change before (Fig. 5e–f and Fig. 6b–d) and after (Fig. 10b and Figs. S12d–e–f) testing, showing the presence of aggregates of nanoparticles with 15–20 nm size.

From the comparison of the EDS elemental maps before (Fig. 6a–b) and after (Fig. 10a–b) testing, we notice that segregation of Fe to the surface did not change over testing. The surface enrichment in Fe can be responsible for the brown color of NiFe8:1–500, which does not change during testing. Further information on the changes that the two different catalysts undergo during testing can be obtained by comparing EDS elemental composition in Table 3. The NiFe8:1–150 catalyst shows an increase in the O content of ca. 4%, suggesting an increase in the oxidation state of the metals, reflected in a decrease of the (Ni+Fe)-to-O atomic ratio from 0.34 to 0.27. A higher O content after testing is consistent with the transformation of  $\text{Ni}(\text{OH})_2$ -like phase to  $\text{NiOOH}$  phase after exposure of the electrode to high OER potentials. This redox transition from Ni(II) to Ni(III) is consistent with the CV peaks in Fig. 1. The presence of areas of  $\text{NiO}_2$  with different levels of protonation, suggested to impart enhanced OER activity by DFT studies [43,105], is also

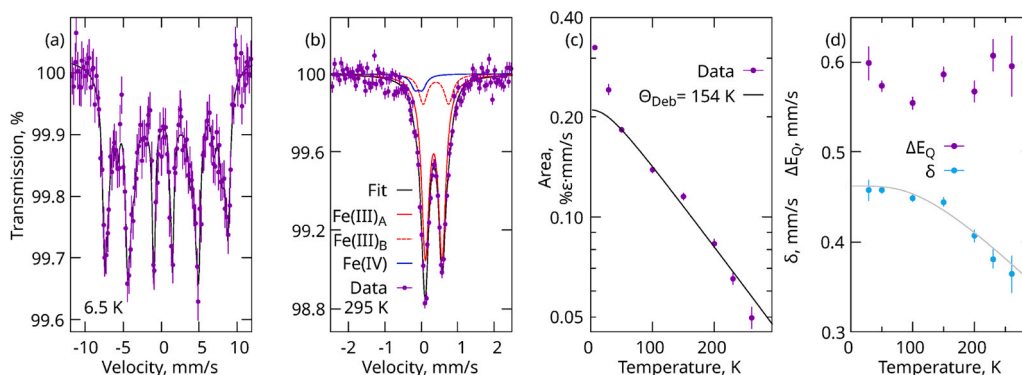


**Fig. 9.** Mössbauer spectral data for the NiFe8:1–150 catalysts. (a) At 6.5 K magnetic hyperfine splitting is observed, (b) at room temperature, two nested doublets of Fe(III) (A and B) and small amount of Fe(IV) is observed. (c) The spectral area for the spectra between 6.5 and 260 K is decreasing rapidly (note the logarithmic scale), indicating a soft lattice, with a Debye temperature of  $\sim 153$  K. (d) The average isomer shift,  $\delta$ , and quadrupole splitting,  $\Delta E_Q$ , from a single doublet fit are indicative of the majority Fe(III) oxidation state. The temperature dependence of the isomer shift indicates a hard lattice ( $\Theta_D \sim 600$  K) for the high-frequency vibrations.

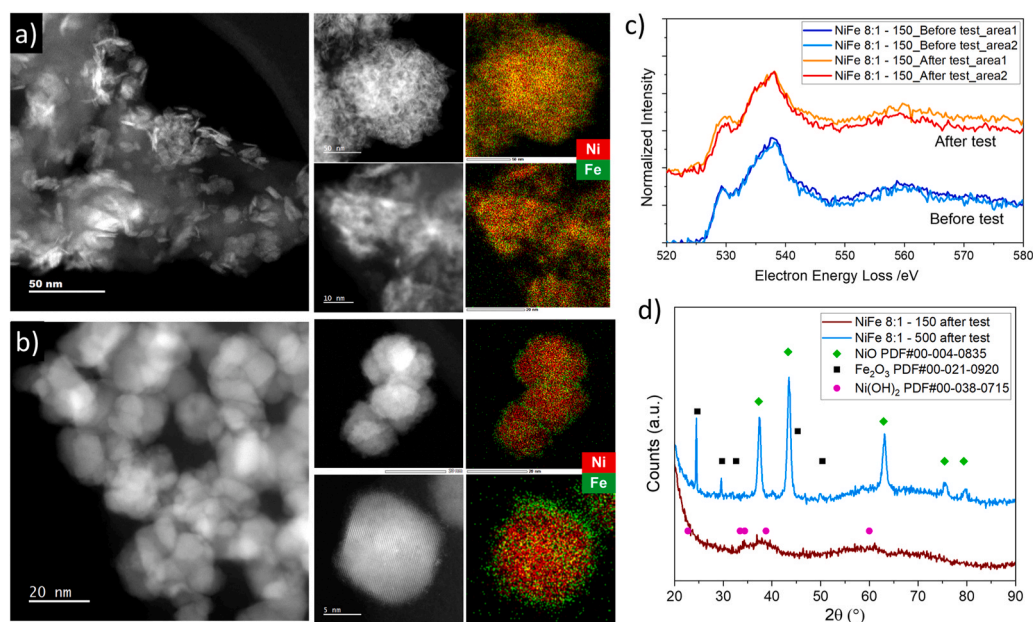


**Fig. 10.** a) High resolution HAADF-STEM image and EDS mapping of Ni and Fe elements on two different areas of the NiFe8:1–150 catalyst after testing. b) High resolution HAADF-STEM image and EDS mapping of Ni and Fe elements on two different areas of the NiFe8:1–500 catalyst after testing. c) EELS of O K-edge on two different areas of the NiFe8:1–150 catalysts after testing. d) XRD spectra of NiFe8:1–150 and NiFe8:1–500 catalysts after testing. Peak positions for reference NiO,  $\text{Fe}_2\text{O}_3$ , and  $\text{Ni}(\text{OH})_2$  are shown for comparison.

possible. The colors of the two standard chemical compounds, green for  $\text{Ni}(\text{OH})_2$  and black for  $\text{NiOOH}$ , also point in this direction. A slight decrease in the Ni-to-Fe atomic ratio from 7.4 before to 6.9 after testing for this catalyst suggests no preferential loss of Fe during testing. The NiFe8:1–500 shows a stable O content (slight decrease of only ca. 1%) and (Ni+Fe)-to-O ratio, suggesting no change in the oxidation state of the metals for this catalyst. However, there is a slight increase of the Ni-to-Fe ratio which can suggest some loss of Fe from this catalyst during testing.

We measured the EELS spectra for the NiFe8:1–150 catalyst after testing and compared with the data for the same catalyst before testing (Fig. 10c). No substantial difference was observed, suggesting that the high degree of disorder is maintained despite the phase change, as confirmed by the STEM images in Fig. 10a and Figs. S12a–b–c that reveal small size, on the order of a few nm, of the platelet-needle-like crystals. These results are also confirmed by XRD of the NiFe8:1–150 catalyst after testing (Fig. 10d), where no peaks are observed. The XRD spectra of

the NiFe8:1–500 catalyst after testing (Fig. 10d) shows the same characteristic peaks of the NiO structure (with some of the features of  $\text{Fe}_2\text{O}_3$ ) also in this case like those observed in the spectrum recorded before testing.

Fig. S13 shows low-resolution STEM images and EDS elemental mapping for the two catalysts after testing, which look similar to the same before testing (Fig. S8). The presence of fluorine (F) in the spectrum in Fig. S13 is due the Nafion binder used for the CL fabrication (uniform distribution over the catalyst particles).

STEM images of the NiFe8:1–150 catalyst deposited on the electrode before the 110-hour durability test (Fig. S14) reveals morphology consistent with that of the catalyst powder. The EDS mapping at higher resolution confirms homogeneous distribution of Ni, Fe and O elements (Fig. S15). After the durability test and consistently with the results of shorter tests, the catalyst shows a structural modification to the platelet-needle-like structure (Fig. S16). Slightly larger such structures seem to form after 110-hour testing than in shorter tests. High-resolution EDS



mapping (Fig. S17) shows homogeneous distribution of Ni, Fe and O also after testing.

Overall, the results of the post-test characterization show that the presence of Ni hydroxide-like small crystallites in the NiFe8:1–150 catalyst facilitates formation of a Ni (oxy)hydroxide layered structure. Conversely, large and stable NiO-like crystallites in NiFe8:1–500 do not undergo substantial structural modification, reflected by their lower OER performance.

It has been reported in the literature that dynamic surface reconstruction is responsible for high OER activity, since the presence of a flexible structure is associated with the ability to accommodate a large amount of oxygen vacancies [106]. Also, it has been reported that the growth of the hydrous Ni(OH)<sub>2</sub>/NiOOH layers upon potential cycling of Ni-Fe oxide materials benefits performance since the formation of hydrous sheeted structures increases accessibility of OH<sup>−</sup> ions (OER reactants) to the active sites, enhancing activity [55]. It has also been suggested that these structural changes may be related to changes in the O concentration (O-to-Ni ratio) in a layered NiO<sub>2</sub>/NiOOH framework occurring during OER, where the intermediate O atoms (oxidized from water molecules) can insert within the layers forming lattice O–O peroxide. However, more investigations are needed to correlate these structural changes with the true OER mechanism on these materials [107].

Therefore, combined with the Fe doping, the observed structural change of the NiFe8:1–150 catalyst is deemed responsible for the high OER activity of this material. Furthermore, the facilitated phase transition from Ni(OH)<sub>2</sub>, an insulator, to the electronically conducting NiOOH [106], can also contribute to the superior electrocatalytic performance of the NiFe8:1–150 catalyst.

#### 4. Conclusions

In this work, we have synthesized and extensively characterized OER electrocatalysts derived from Ni-Fe oxides aerogels. We have investigated the impact of synthesis variables such as the Ni-to-Fe ratio, the addition of a third transition metal (Co, Mn), and the heat-treatment temperature on the OER activity. The heat-treatment temperature in particular impacts both the catalyst structure and OER activity in alkaline media. We investigated more in detail two catalysts derived from the same aerogel precursor having a Ni-to-Fe atomic ratio of 8:1, heat-treated at different temperatures, 150 °C and 500 °C. These heat treatments yielded materials with substantially different morphology and structure. The material heat-treated at 150 °C, named NiFe8:1–150, showed a disordered structure with small crystallites of 1–2 nm size evidenced by high-resolution STEM, but not detectable by XRD, and large surface area and pore volume (> 380 m<sup>2</sup> g<sup>−1</sup> and 0.85 cm<sup>3</sup> g<sup>−1</sup>), like those of the aerogel precursor. The material heat-treated at 500 °C, named NiFe8:1–500, showed much lower surface area and pore volume, 55 m<sup>2</sup> g<sup>−1</sup> and 0.2 cm<sup>3</sup> g<sup>−1</sup>, respectively, and larger crystallites (15–20 nm) with a NiO crystalline structure. The different degrees of structural order were also evidenced by the EELS spectra.

Bulk chemical composition analysis by EDS evidenced similar Ni-to-Fe ratio in both catalysts, matching the nominal value used for the synthesis, but higher oxygen content for the NiFe8:1–150 catalyst. Near-surface chemical composition characterization (XPS) also revealed a higher oxygen content for the NiFe8:1–150 catalyst, and a higher Fe content, which is also confirmed by the EDS mapping. Mössbauer spectroscopy results for the NiFe8:1–150 catalyst revealed a soft lattice compatible with the aerogel structure, with Fe predominantly in the Fe (III) oxidation state, and intimately mixed at the atomic scale within the Ni(OH)<sub>2</sub> structure.

XAFS analysis confirmed Fe predominantly in Fe(III) form for the NiFe8:1–150 catalyst. XAFS analysis also confirmed NiO-like structure for the NiFe8:1–500 catalyst, while a higher coordination number was observed for the NiFe8:1–150 catalyst, compatible with a more hydrated structure, confirming microscopy, EDS, XRD, and XPS results.

The two catalysts showed substantially different OER activity in a three-electrode cell (RDE) with the NiFe8:1–150 being much more active than the NiFe8:1–500. This OER activity gap resulted in a large performance difference when the catalysts were applied to the anode of an operating AEMWE, with both pure water and supporting electrolyte feeding. While showing a better performance, the NiFe8:1–150 catalyst required a longer activation procedure. This catalyst also showed a superior performance in an AEMWE fed with 1 M KOH when compared to commercial NiFe<sub>2</sub>O<sub>4</sub> material, as well as a degradation rate below 0.5 mV/h over 110 h at 1 A cm<sup>−2</sup>.

The post-test characterizations showed that the NiFe8:1–150 catalyst underwent a substantial structural modification, with the formation of platelet-needle-shaped small crystals, associated with a change of color from greenish-yellowish to black. On the other hand, the NiFe8:1–500 catalyst did not show any noticeable structural modification over testing.

In summary, the presence of small crystallites in the aerogel-derived catalyst heat-treated at the lower of two temperatures (150 °C) facilitates the formation of a Ni (oxy)hydroxide layered structure, resulting in superior OER activity. The larger NiO-like crystals formed in the catalyst heat-treated at the high temperature (500 °C) do not easily undergo this transition, leading to much lower OER performance.

#### CRedit authorship contribution statement

**Osmieri Luigi:** Conceptualization, Formal analysis, Investigation, Methodology, Resources, Visualization, Writing – original draft, Writing – review & editing. **Yu Haoran:** Formal analysis, Investigation, Visualization, Writing – review & editing. **Hermann Raphaël P.:** Formal analysis, Investigation, Visualization, Writing – review & editing. **Kreider Melissa E.:** Formal analysis, Investigation, Validation, Writing – review & editing. **Meyer Harry M.:** Formal analysis, Investigation. **Kropf Jeremy A.:** Formal analysis, Investigation. **Park Jae Hyung:** Formal analysis, Investigation. **Alia Shaun M.:** Formal analysis, Project administration, Supervision. **Cullen David A.:** Formal analysis, Funding acquisition, Project administration, Supervision. **Myers Deborah J.:** Formal analysis, Funding acquisition, Project administration, Supervision, Visualization, Writing – review & editing. **Zelenay Piotr:** Funding acquisition, Project administration, Supervision, Writing – review & editing.

#### Declaration of Competing Interest

The authors declare that they have no known competing financial interests or personal relationships that could have appeared to influence the work reported in this work.

#### Data Availability

Data will be made available on request.

#### Acknowledgments

Financial support was provided by the U.S. DOE Office of Energy Efficiency and Renewable Energy, Hydrogen and Fuel Cell Technologies Office, under the ElectroCat Consortium, DOE technology managers McKenzie Hubert and William Gibbons, and DOE program managers David Peterson and Dimitrios Papageorgopoulos. Funding was also provided by the Los Alamos National Laboratory Directed Research & Development (LDRD) project 20210953PRD3. This work was authored in part by Los Alamos National Laboratory operated by Triad National Security, LLC under US DOE contract no. 89233218CNA000001, by Oak Ridge National Laboratory operated by UT-Battelle, LLC, under contract no. DE-AC05-00OR22725, by Argonne National Laboratory, a DOE Office of Science Laboratory managed by the University of Chicago Argonne, LLC under contract no. DE-AC-02-06CH11357, and by the



National Renewable Energy Laboratory, operated by Alliance for Sustainable Energy, LLC, for the U.S. Department of Energy (DOE) under Contract No. DE-AC36-08GO28308. STEM research conducted as part of a user project at the Center for Nanophase Materials Sciences (CNMS), which is a US Department of Energy, Office of Science User Facility at Oak Ridge National Laboratory. This research used the resources of the Advanced Photon Source (APS), a U.S. DOE Office of Science User Facility operated for the DOE Office of Science by Argonne National Laboratory under Contract No. DE-AC02-06CH11357. X-ray absorption spectroscopy data were acquired at MRCAT at the APS. MRCAT operations are supported by the Department of Energy and the MRCAT member institutions.

Edward F. Holby from Theoretical Division at Los Alamos National Laboratory is acknowledged for fruitful discussion.

The views expressed in the article do not necessarily represent the views of the DOE or the U.S. Government. The U.S. Government retains and the publisher, by accepting the article for publication, acknowledges that the U.S. Government retains a nonexclusive, paid-up, irrevocable, worldwide license to publish or reproduce the published form of this work, or allow others to do so, for U.S. Government purposes.

## Appendix A. Supporting information

Supplementary data associated with this article can be found in the online version at [doi:10.1016/j.apcatb.2024.123843](https://doi.org/10.1016/j.apcatb.2024.123843).

## References

- [1] H.L. van Soest, M.G.J. den Elzen, D.P. van Vuuren, Net-zero emission targets for major emitting countries consistent with the Paris agreement, *Nat. Commun.* 12 (1) (2021) 9, <https://doi.org/10.1038/s41467-021-22294-x>.
- [2] J. Rogelj, M. Schaeffer, M. Meinshausen, R. Knutti, J. Alcamo, K. Riahi, W. Hare, Zero emission targets as long-term global goals for climate protection, *Environ. Res. Lett.* 10 (2015), <https://doi.org/10.1088/1748-9326/10/10/105007>.
- [3] Electric Power Annual, U.S. Energy Inf. Adm. (2022). (<https://www.eia.gov/electricity/annual/%0A>).
- [4] S. Wang, B. Tarroja, L.S. Schell, B. Shaffer, S. Samuelsen, Prioritizing among the end uses of excess renewable energy for cost-effective greenhouse gas emission reductions, *Appl. Energy* 235 (2019) 284–298, <https://doi.org/10.1016/j.apenergy.2018.10.071>.
- [5] B. Pivovar, N. Rustagi, S. Satyapal, Hydrogen at scale (H2@Scale) key to a clean, economic, and sustainable energy system, *Electrochem. Soc. Interface* 27 (2018) 47–52. ([https://www.electrochem.org/dl/interface/wtr/wtr08/wtr08\\_p40-45.pdf%0Ahttps://techcrunch.com/2017/03/01/facebook-brings-suicide-prevention-tools-to-live-and-messenger/](https://www.electrochem.org/dl/interface/wtr/wtr08/wtr08_p40-45.pdf%0Ahttps://techcrunch.com/2017/03/01/facebook-brings-suicide-prevention-tools-to-live-and-messenger/)).
- [6] A.M. Oliveira, R.R. Beswick, Y. Yan, A green hydrogen economy for a renewable energy society, *Curr. Opin. Chem. Eng.* 33 (2021) 100701, <https://doi.org/10.1016/j.coche.2021.100701>.
- [7] A. Velazquez Abad, P.E. Dodds, Green hydrogen characterisation initiatives: Definitions, standards, guarantees of origin, and challenges, *Energy Policy* 138 (2020) 111300, <https://doi.org/10.1016/j.enpol.2020.111300>.
- [8] A. Kusoglu, Chalkboard 1 - The many colors of hydrogen, *Electrochem. Soc. Interface* 30 (2021) 44–48.
- [9] H.A. Miller, K. Bouzek, J. Hnat, S. Loos, C.I. Bernäcker, T. Weißgärber, L. Röntzsch, J. Meier-Haack, Green hydrogen from anion exchange membrane water electrolysis: a review of recent developments in critical materials and operating conditions, *Sustain. Energy Fuels* 4 (2020) 2114–2133, <https://doi.org/10.1039/c9se01240k>.
- [10] A. Buttler, H. Spliethoff, Current status of water electrolysis for energy storage, grid balancing and sector coupling via power-to-gas and power-to-liquids: a review, *Renew. Sustain. Energy Rev.* 82 (2018) 2440–2454, <https://doi.org/10.1016/j.rser.2017.09.003>.
- [11] D. Li, E.J. Park, W. Zhu, Q. Shi, Y. Zhou, H. Tian, Y. Lin, A. Serov, B. Zulevi, E. D. Baca, C. Fujimoto, H.T. Chung, Y.S. Kim, Highly quaternized polystyrene ionomers for high performance anion exchange membrane water electrolyzers, *Nat. Energy* 5 (2020) 378–385, <https://doi.org/10.1038/s41560-020-0577-x>.
- [12] A.Y. Faid, S. Sunde, Anion exchange membrane water electrolysis from catalyst design to the membrane electrode assembly, *Energy Technol.* 10 (2022), <https://doi.org/10.1002/ente.202200506>.
- [13] M. Schalenbach, G. Tjarks, M. Carmo, W. Lueke, M. Mueller, D. Stolten, Acidic or Alkaline? Towards a new perspective on the efficiency of water electrolysis, *J. Electrochem. Soc.* 163 (2016) F3197–F3208, <https://doi.org/10.1149/2.0271611jes>.
- [14] C. Santoro, A. Lavacchi, P. Mustarelli, V. Di Noto, L. Elbaz, D. Dekel, F. Jaouen, What is next in anion-exchange membrane water electrolyzers? Bottlenecks, benefits, and future, 202200027, *ChemSusChem* (2022), <https://doi.org/10.1002/cssc.202200027>.
- [15] C. Karacan, F.P. Lohmann-Richters, M. Shviro, G.P. Keeley, M. Müller, M. Carmo, D. Stolten, Fabrication of high performing and durable nickel-based catalyst coated diaphragms for alkaline water electrolyzers, *J. Electrochem. Soc.* 169 (2022) 054502, <https://doi.org/10.1149/1945-7111/ac697f>.
- [16] G. Bender, M. Carmo, T. Smolinka, A. Gago, N. Danilovic, M. Mueller, F. Ganci, A. Fallisch, P. Lettenmeier, K.A. Friedrich, K. Ayers, B. Pivovar, J. Mergel, D. Stolten, Initial approaches in benchmarking and round robin testing for proton exchange membrane water electrolyzers, *Int. J. Hydrog. Energy* 44 (2019) 9174–9187, <https://doi.org/10.1016/j.ijhydene.2019.02.074>.
- [17] M. Carmo, D.L. Fritz, J. Mergel, D. Stolten, A comprehensive review on PEM water electrolysis, *Int. J. Hydrog. Energy* 38 (2013) 4901–4934, <https://doi.org/10.1016/j.ijhydene.2013.01.151>.
- [18] J. Xu, J. Li, Z. Lian, A. Araujo, Y. Li, B. Wei, Z. Yu, O. Bondarchuk, I. Amorim, V. Tileli, B. Li, L. Liu, Atomic-step enriched ruthenium–iridium nanocrystals anchored homogeneously on MOF-derived support for efficient and stable oxygen evolution in acidic and neutral media, *ACS Catal.* 11 (2021) 3402–3413, <https://doi.org/10.1021/acscatal.0c04117>.
- [19] K.A. Friedrich, P. Lettenmeier, A.S. Ansar, L. Wang, A.S. Gago, Achieving cost reduction in PEM electrolysis by material development, 6th Eur PEFC Electrolyse Forum, 2017, , 31–40.
- [20] R.J. Ouimet, J.R. Glenn, D. De Porcellinis, A.R. Motz, M. Carmo, K.E. Ayers, The Role of Electrocatalysts in the Development of Gigawatt-Scale PEM Electrolyzers, *ACS Catal.* (2022) 6159–6171, <https://doi.org/10.1021/acscatal.2c00570>.
- [21] Q. Liang, G. Brocks, A. Biebele-Hütter, Oxygen evolution reaction (OER) mechanism under alkaline and acidic conditions, *J. Phys. Energy* 3 (2021), <https://doi.org/10.1088/2515-7655/abdc85>.
- [22] C. Liu, M. Carmo, G. Bender, A. Everwand, T. Lickert, J.L. Young, T. Smolinka, D. Stolten, W. Lehnert, Performance enhancement of PEM electrolyzers through iridium-coated titanium porous transport layers, *Electrochem. Commun.* 97 (2018) 96–99, <https://doi.org/10.1016/j.elecom.2018.10.021>.
- [23] Johnson Matthey, (n.d.). (<http://www.platinum.matthey.com/prices>) (accessed October 9, 2023).
- [24] C. Minke, M. Suermann, B. Bensmann, R. Hanke-Rauschenbach, Is iridium demand a potential bottleneck in the realization of large-scale PEM water electrolysis? *Int. J. Hydrog. Energy* 46 (2021) 23581–23590, <https://doi.org/10.1016/j.ijhydene.2021.04.174>.
- [25] D. Henkensmeier, M. Najibah, C. Harms, J. Žitka, J. Hnat, K. Bouzek, Overview: state-of-the-art commercial membranes for anion exchange membrane water electrolysis, *J. Electrochem. Energy Convers. Storage* 18 (2021), <https://doi.org/10.1115/1.4047963>.
- [26] D. Li, A.R. Motz, C. Bae, C. Fujimoto, G. Yang, F.Y. Zhang, K.E. Ayers, Y.S. Kim, Durability of anion exchange membrane water electrolyzers, *Energy Environ. Sci.* 14 (2021) 3393–3419, <https://doi.org/10.1039/d0ee04086j>.
- [27] G.A. Lindquist, S.Z. Oener, R. Krivina, A.R. Motz, A. Keane, C. Capuano, K. E. Ayers, S.W. Boettcher, Performance and durability of pure-water-fed anion exchange membrane electrolyzers using baseline materials and operation, *ACS Appl. Mater. Interfaces* 13 (2021) 51917–51924, <https://doi.org/10.1021/acsaami.1c06053>.
- [28] J. Huang, Z. Yu, J. Tang, P. Wang, Q. Tan, J. Wang, X. Lei, A review on anion exchange membranes for fuel cells: Anion-exchange polyelectrolytes and synthesis strategies, *Int. J. Hydrog. Energy* 47 (2022) 27800–27820, <https://doi.org/10.1016/j.ijhydene.2022.06.140>.
- [29] R.A. Krivina, G.A. Lindquist, S.R. Beaudoin, T.N. Stovall, L. Willow, R.A. Krivina, G.A. Lindquist, S.R. Beaudoin, T.N. Stovall, W.L. Thompson, S.W. Boettcher, Anode Catalysts in anion-exchange-membrane electrolysis without supporting electrolyte: conductivity, dynamics, and ionomer degradation, *Adv. Mater.* 2203033 (2022) 1–10, <https://doi.org/10.1002/adma.22203033>.
- [30] L. Osmieri, Y. He, H.T. Chung, G. McCool, B. Zulevi, D.A. Cullen, P. Zelenay, La-Sr-Co Oxide Catalysts for oxygen evolution reaction in anion exchange membrane water electrolyzers: the role of electrode fabrication on performance and durability, *J. Power Sources* 556 (2023) 232484, <https://doi.org/10.1016/j.jpowsour.2022.232484>.
- [31] E. Frackowiak, F. Béguin, Carbon materials for the electrochemical storage of energy in capacitors, *Carbon* 39 (2001) 937–950, [https://doi.org/10.1016/S0008-6223\(00\)00183-4](https://doi.org/10.1016/S0008-6223(00)00183-4).
- [32] L. Osmieri, R. Escudero-Cid, M. Armandi, A.H.A. Monteverde Videla, J.L. G. Fierro, P. Ocón, S. Specchia, Fe-N/C catalysts for oxygen reduction reaction supported on different carbonaceous materials. Performance in acidic and alkaline direct alcohol fuel cells, *Appl. Catal. B Environ.* 205 (2017) 637–653, <https://doi.org/10.1016/j.apcatb.2017.01.003>.
- [33] H. Wang, L.R. Grabstanowicz, H.M. Barkholtz, D. Rebollar, Z.B. Kaiser, D. Zhao, B.H. Chen, D.J. Liu, Impacts of imidazolate ligand on performance of zeolitic-imidazolate framework-derived oxygen reduction catalysts, *ACS Energy Lett.* 4 (2019) 2500–2507, <https://doi.org/10.1021/acsenergylett.9b01740>.
- [34] Y. Yi, G. Weinberg, M. Prenzler, M. Greiner, S. Heumann, S. Becker, R. Schlögl, Electrochemical corrosion of a glassy carbon electrode, *Catal. Today* 295 (2017) 32–40, <https://doi.org/10.1016/j.cattod.2017.07.013>.
- [35] N. Macauley, D.D. Papadakis, J. Fairweather, D. Spennak, D. Langlois, R. Ahluwalia, K.L. More, R. Mukundan, R.L. Borup, Carbon corrosion in PEM fuel cells and the development of accelerated stress tests, *J. Electrochem. Soc.* 165 (2018) F3148–F3160, <https://doi.org/10.1149/2.0061806jes>.
- [36] J.L. Young, Z. Kang, F. Ganci, S. Madachy, G. Bender, PEM electrolyzer characterization with carbon-based hardware and material sets, *Electrochem. Commun.* 124 (2021) 106941, <https://doi.org/10.1016/j.elecom.2021.106941>.
- [37] J. Suntivich, K.J. May, H.A. Gasteiger, J.B. Goodenough, Y. Shao-horn, A perovskite oxide optimized for oxygen evolution catalysis from molecular

- orbital principles, *Science* 334 (2011) 2010–2012. (<http://www.sciencemag.org/cgi/doi/10.1126/science.1212858>).
- [38] S. Fu, J. Song, C. Zhu, G.L. Xu, K. Amine, C. Sun, X. Li, M.H. Engelhard, D. Du, Y. Lin, Ultrafine and highly disordered Ni<sub>2</sub>Fe<sub>1</sub> nanofoams enabled highly efficient oxygen evolution reaction in alkaline electrolyte, *Nano Energy* 44 (2018) 319–326, <https://doi.org/10.1016/j.nanoen.2017.12.010>.
  - [39] E. Fabbri, M. Nachttegaal, T. Binniger, X. Cheng, B.J. Kim, J. Durst, F. Bozza, T. Graule, R. Schäublin, L. Wiles, M. Pertoso, N. Danilovic, K.E. Ayers, T. J. Schmidt, Dynamic surface self-reconstruction is the key of highly active perovskite nano-electrocatalysts for water splitting, *Nat. Mater.* 16 (2017) 925–931, <https://doi.org/10.1038/nmat4938>.
  - [40] K. Wang, X. Wang, Z. Li, B. Yang, M. Ling, X. Gao, J. Lu, Q. Shi, L. Lei, G. Wu, Y. Hou, Designing 3d dual transition metal electrocatalysts for oxygen evolution reaction in alkaline electrolyte: beyond oxides, *Nano Energy* 77 (2020) 105162, <https://doi.org/10.1016/j.nanoen.2020.105162>.
  - [41] O. Diaz-Morales, D. Ferrus-Suspedra, M.T.M. Koper, The importance of nickel oxyhydroxide deprotonation on its activity towards electrochemical water oxidation, *Chem. Sci.* 7 (2016) 2639–2645, <https://doi.org/10.1039/c5sc04486c>.
  - [42] J.Y.C. Chen, L. Dang, H. Liang, W. Bi, J.B. Gerken, S. Jin, E.E. Alp, S.S. Stahl, Operando analysis of NiFe and Fe oxyhydroxide electrocatalysts for water oxidation: detection of Fe<sup>4+</sup> by Mössbauer spectroscopy, *J. Am. Chem. Soc.* 137 (2015) 15090–15093, <https://doi.org/10.1021/jacs.5b10699>.
  - [43] V. Fidelesky, M.C. Toroker, Enhanced water oxidation catalysis of nickel oxyhydroxide through the addition of vacancies, *J. Phys. Chem. C* 120 (2016) 25405–25410, <https://doi.org/10.1021/acs.jpcc.6b07931>.
  - [44] R. Subbaraman, D. Tripkovic, K.C. Chang, D. Strmcnik, A.P. Paulikas, P. Hirsunsi, M. Chan, J. Greeley, V. Stamenkovic, N.M. Markovic, Trends in activity for the water electrolyser reactions on 3d M(Ni,Co,Fe,Mn) hydroxide catalysts, *Nat. Mater.* 11 (2012) 550–557, <https://doi.org/10.1038/nmat3313>.
  - [45] V. Fidelesky, D. Furman, Y. Khodorkovsky, Y. Elbaz, Y. Zeiri, M.C. Toroker, Electronic structure of  $\beta$ -NiOOH with hydrogen vacancies and implications for energy conversion applications, *MRS Commun.* 7 (2017) 206–213, <https://doi.org/10.1557/mrc.2017.26>.
  - [46] D.S. Hall, D.J. Lockwood, C. Bock, B.R. MacDougall, Nickel hydroxides and related materials: a review of their structures, synthesis and properties, *Proc. R. Soc. A Math. Phys. Eng. Sci.* 471 (2015), <https://doi.org/10.1098/rspa.2014.0792>.
  - [47] R. Barnard, C.F. Randell, F.L. Tye, Studies concerning charged nickel hydroxide electrodes I. Measurement of reversible potentials, *J. Appl. Electrochem.* 10 (1980) 109–125, <https://doi.org/10.1007/BF00937345>.
  - [48] W. Moschcowitsch, N. Zion, H.C. Honig, N. Levy, D.A. Cullen, L. Elbaz, Mixed-metal nickel – iron oxide aerogels for oxygen evolution reaction, *ACS Catal.* (2022), <https://doi.org/10.1021/acscatal.2c03351>.
  - [49] S. Klaus, Y. Cai, M.W. Louie, L. Trotochaud, A.T. Bell, Effects of Fe electrolyte impurities on Ni(OH)<sub>2</sub>/NiOOH structure and oxygen evolution activity, *J. Phys. Chem. C* 119 (2015) 7243–7254, <https://doi.org/10.1021/acs.jpcc.5b00105>.
  - [50] L. Trotochaud, S.L. Young, J.K. Ranney, S.W. Boettcher, Nickel-Iron oxyhydroxide oxygen-evolution electrocatalysts: the role of intentional and incidental iron incorporation, *J. Am. Chem. Soc.* 136 (2014) 6744–6753, <https://doi.org/10.1021/ja502379c>.
  - [51] M.B. Stevens, C.D.M. Trang, L.J. Enman, J. Deng, S.W. Boettcher, Reactive Fe-sites in Ni/Fe (Oxy)hydroxide are responsible for exceptional oxygen electrocatalysis activity, *J. Am. Chem. Soc.* 139 (2017) 11361–11364, <https://doi.org/10.1021/jacs.7b07117>.
  - [52] D. Xu, M.B. Stevens, M.R. Cosby, S.Z. Oener, A.M. Smith, L.J. Enman, K.E. Ayers, C.B. Capuano, J.N. Renner, N. Danilovic, Y. Li, H. Wang, Q. Zhang, S. W. Boettcher, Earth-abundant oxygen electrocatalysts for alkaline anion-exchange-membrane water electrolysis: effects of catalyst conductivity and comparison with performance in three-electrode cells, *ACS Catal.* 9 (2019) 7–15, <https://doi.org/10.1021/acscatal.8b04001>.
  - [53] Q. He, Y. Wan, H. Jiang, Z. Pan, C. Wu, M. Wang, X. Wu, B. Ye, P.M. Ajayan, L. Song, Nickel vacancies boost reconstruction in nickel hydroxide electrocatalyst, *ACS Energy Lett.* 3 (2018) 1373–1380, <https://doi.org/10.1021/acsenergylett.8b00515>.
  - [54] D. Drevon, M. Görlin, P. Chernev, L. Xi, H. Dau, K.M. Lange, Uncovering the role of oxygen in Ni-Fe(OxHy) electrocatalysts using in situ soft X-ray absorption spectroscopy during the oxygen evolution reaction, *Sci. Rep.* 9 (1) (2019) 11, <https://doi.org/10.1038/s41598-018-37307-x>.
  - [55] D.F. Abbott, E. Fabbri, M. Borlaf, F. Bozza, R. Schäublin, M. Nachttegaal, T. Graule, T.J. Schmidt, Operando X-ray absorption investigations into the role of Fe in the electrochemical stability and oxygen evolution activity of Ni<sub>1-x</sub>Fe<sub>x</sub>Oy nanoparticles, *J. Mater. Chem. A* 6 (2018) 24534–24549, <https://doi.org/10.1039/c8ta09336a>.
  - [56] J.H. Shah, Q.X. Xie, Z.C. Kuang, R. Le Ge, W.H. Zhou, D.R. Liu, A.I. Rykov, X. N. Li, J.S. Luo, J.H. Wang, In situ/operando 57Fe Mössbauer spectroscopy technique and its applications in nife based electrocatalysts for oxygen evolution reaction, *J. Electrochem.* 28 (2022) 1–31, <https://doi.org/10.13208/j.electrochem.210854>.
  - [57] Z. Yu, Y. Bai, G. Tsekouras, Z. Cheng, Recent advances in Ni-Fe (Oxy)hydroxide electrocatalysts for the oxygen evolution reaction in alkaline electrolyte targeting industrial applications, *Nano Sel.* 3 (2022) 766–791, <https://doi.org/10.1002/nano.202100286>.
  - [58] A. Badreldin, A.E. Abusrafa, A. Abdel-Wahab, Oxygen-deficient perovskites for oxygen evolution reaction in alkaline media: a review, *Emergent Mater.* 3 (2020) 567–590, <https://doi.org/10.1007/s42247-020-00123-z>.
  - [59] A.E. Gash, J.H. Satcher, R.L. Simpson, Monolithic nickel(II)-based aerogels using an organic epoxide: the importance of the counterion, *J. Non Cryst. Solids* 350 (2004) 145–151, <https://doi.org/10.1016/j.jnoncrysol.2004.06.030>.
  - [60] J. Xiao, A.M. Oliveira, L. Wang, Y. Zhao, T. Wang, J. Wang, B.P. Setzler, Y. Yan, Water-fed hydroxide exchange membrane electrolyzer enabled by a fluoride-incorporated nickel-iron oxyhydroxide oxygen evolution electrode, *ACS Catal.* 11 (2021) 264–270, <https://doi.org/10.1021/acscatal.0c04200>.
  - [61] L. Wan, J. Liu, Z. Xu, Q. Xu, M. Pang, P. Wang, B. Wang, Construction of integrated electrodes with transport highways for pure-water-fed anion exchange membrane water electrolysis, *Small* 18 (2022), <https://doi.org/10.1002/sml.202200380>.
  - [62] S.C. Zignani, M. Lo Faro, S. Trocino, A.S. Arico, Investigation of NiFe-based catalysts for oxygen evolution in anion-exchange membrane electrolysis, *Energies* 13 (2020), <https://doi.org/10.3390/en13071720>.
  - [63] J.E. Park, H.J. Choi, S.Y. Kang, G.Y. Jang, O.H. Kim, M. Karuppannan, Y.E. Sung, O.J. Kwon, Y.H. Cho, Effect of pore structures in nickel-based porous transport layers for high-performance and durable anion-exchange membrane water electrolysis, *Int. J. Energy Res.* (2022) 16670–16678, <https://doi.org/10.1002/er.8331>.
  - [64] K.W. Ahmed, M.J. Jang, S. Habibpour, Z. Chen, M. Fowler, NiFeOx and NiFeCoOx catalysts for anion exchange membrane water electrolysis, *Electrochemistry* 3 (2022) 843–861, <https://doi.org/10.3390/electrochem3040055>.
  - [65] S.S. Jeon, J. Lim, P.W. Kang, J.W. Lee, G. Kang, H. Lee, Design principles of NiFe-layered double hydroxide anode catalysts for anion exchange membrane water electrolyzers, *ACS Appl. Mater. Interfaces* 13 (2021) 37179–37186, <https://doi.org/10.1021/acsami.1c09606>.
  - [66] A.E. Gash, T.M. Tillotson, J.H. Satcher, J.F. Poco, L.W. Hrubesh, R.L. Simpson, Use of epoxides in the sol-gel synthesis of porous iron(III) oxide monoliths from Fe(III) salts, *Chem. Mater.* 13 (2001) 999–1007, <https://doi.org/10.1021/cm0007611>.
  - [67] Q. Gao, X. Wang, Z. Shi, Z. Ye, W. Wang, N. Zhang, Z. Hong, M. Zhi, Synthesis of porous NiCo<sub>2</sub>S<sub>4</sub> aerogel for supercapacitor electrode and oxygen evolution reaction electrocatalyst, *Chem. Eng. J.* 331 (2018) 185–193, <https://doi.org/10.1016/j.cej.2017.08.067>.
  - [68] S. Yan, M. Zhong, C. Wang, X. Lu, Amorphous aerogel of trimetallic FeCoNi alloy for highly efficient oxygen evolution, *Chem. Eng. J.* 430 (2022) 132955, <https://doi.org/10.1016/j.cej.2021.132955>.
  - [69] A. Du, B. Zhou, J. Shen, S. Xiao, Z. Zhang, C. Liu, M. Zhang, Monolithic copper oxide aerogel via dispersed inorganic sol-gel method, *J. Non Cryst. Solids* 355 (2009) 175–181, <https://doi.org/10.1016/j.jnoncrysol.2008.11.015>.
  - [70] J. Suntivich, H.A. Gasteiger, N. Yabuuchi, Y. Shao-Horn, Electrochemical measurement methodology of oxide catalysts using a thin-film rotating disk electrode, *J. Electrochem. Soc.* 157 (2010) B1263, <https://doi.org/10.1149/1.3456630>.
  - [71] J. Chlistunoff, RRDE and voltammetric study of ORR on pyrolyzed Fe / polyaniline catalyst. On the origins of variable tafel slopes, *J. Phys. Chem. C* 115 (2011) 6496–6507.
  - [72] L. Osmieri, A.H.A. Monteverde Videla, P. Ocon, S. Specchia, Kinetics of oxygen electroreduction on Me-N-C (Me = Fe, Co, Cu) catalysts in acidic medium. Insights on the effect of the transition metal, *J. Phys. Chem. C* 121 (2017) 17796–17817, <https://doi.org/10.1021/acs.jpcc.7b02455>.
  - [73] I.M. Sadiek, A.M. Mohammad, M.E. El-Shakre, M.S. El-Deab, Electrochemical activity of nickel oxide nanoparticles-modified electrodes: optimization of the loading level and operating pH towards the oxygen evolution reaction, *Int. J. Hydrog. Energy* 37 (2012) 68–77, <https://doi.org/10.1016/j.ijhydene.2011.09.097>.
  - [74] X. Deng, D.C. Soreescu, I. Waluyo, A. Hunt, D.R. Kauffman, Bulk vs intrinsic activity of NiFeOx electrocatalysts in the oxygen evolution reaction: the influence of catalyst loading, morphology, and support material, *ACS Catal.* 10 (2020) 11768–11778, <https://doi.org/10.1021/acscatal.0c03109>.
  - [75] B. Beden, D. Floner, J.M. Léger, C. Lamy, A voltammetric study of the formation on hydroxides and oxyhydroxides on nickel single crystal electrodes in contact with an alkaline solution, *Surf. Sci.* 162 (1985) 822–829, [https://doi.org/10.1016/0039-6028\(85\)90985-9](https://doi.org/10.1016/0039-6028(85)90985-9).
  - [76] W. Moschcowitsch, K. Dhaka, S. Gonen, R. Attias, Y. Tsur, M. Caspari Toroker, L. Elbaz, Ternary NiFeTiOOH catalyst for the oxygen evolution reaction: study of the effect of the addition of Ti at different loadings, *ACS Catal.* 10 (2020) 4879–4887, <https://doi.org/10.1021/acscatal.0c00105>.
  - [77] S.M. Alia, N. Danilovic, Rotating disk electrode standardization and best practices in acidic oxygen evolution for low-temperature electrolysis, *Front. Energy Res.* 10 (2022) 1–8, <https://doi.org/10.3389/fenrg.2022.857663>.
  - [78] G.C. Anderson, B.S. Pivovar, S.M. Alia, Establishing performance baselines for the oxygen evolution reaction in alkaline electrolytes, *J. Electrochem. Soc.* 167 (2020) 044503, <https://doi.org/10.1149/1945-7111/ab7090>.
  - [79] J. Suntivich, K.J. May, H.A. Gasteiger, J.B. Goodenough, Y. Shao-Horn, A perovskite oxide optimized for oxygen evolution catalysis from molecular orbital principles, *Sci.* (80-) 334 (2011) 1383–1385, <https://doi.org/10.1126/science.1212858>.
  - [80] M.S. Burke, L.J. Enman, A.S. Batchellor, S. Zou, S.W. Boettcher, Oxygen evolution reaction electrocatalysis on transition metal oxides and (oxy) hydroxides: activity trends and design principles, *J. Chem. Mater.* 27 (2015) 7549–7558, <https://doi.org/10.1021/acs.chemmater.5b03148>.
  - [81] N.U. Hassan, Y. Zheng, P.A. Kohl, W.E. Mustain, KOH vs deionized water operation in anion exchange membrane electrolyzers, *J. Electrochem. Soc.* 169 (2022) 044526, <https://doi.org/10.1149/1945-7111/ac5f1d>.

- [82] A. Kiessling, J.C. Fornaciari, G. Anderson, X. Peng, A. Gerstmayr, M.R. Gerhardt, S. McKinney, A. Serov, Y.S. Kim, B. Zulevi, A.Z. Weber, N. Danilovic, Influence of supporting electrolyte on hydroxide exchange membrane water electrolysis performance: anolyte, *J. Electrochem. Soc.* 168 (2021) 084512, <https://doi.org/10.1149/1945-7111/ac1dcd>.
- [83] A.W. Tricker, J.K. Lee, J.R. Shin, N. Danilovic, A.Z. Weber, X. Peng, Design and operating principles for high-performing anion exchange membrane water electrolyzers, *J. Power Sources* 567 (2023) 232967, <https://doi.org/10.1016/j.jpowsour.2023.232967>.
- [84] K. Li, S. Yu, D. Li, L. Ding, W. Wang, Z. Xie, E.J. Park, C. Fujimoto, D.A. Cullen, Y. S. Kim, F.-Y. Zhang, Engineered thin diffusion layers for anion-exchange membrane electrolyzer cells with outstanding performance, *ACS Appl. Mater. Interfaces* 13 (2021) 50957–50964, <https://doi.org/10.1021/acsami.1c14693>.
- [85] N.U. Hassan, M. Mandal, B. Zulevi, P.A. Kohl, W.E. Mustain, Understanding and improving anode performance in an alkaline membrane electrolyzer using statistical design of experiments, *Electrochim. Acta* 409 (2022) 140001, <https://doi.org/10.1016/j.electacta.2022.140001>.
- [86] N.U. Hassan, E. Motyka, J. Kweder, P. Ganesan, B. Brechin, B. Zulevi, H.R. Colón-Mercado, P.A. Kohl, W.E. Mustain, Effect of porous transport layer properties on the anode electrode in anion exchange membrane electrolyzers, *J. Power Sources* 555 (2023) 1–12, <https://doi.org/10.1016/j.jpowsour.2022.232371>.
- [87] J. Liu, Z. Kang, D. Li, M. Pak, S.M. Alia, C. Fujimoto, G. Bender, Y.S. Kim, A. Z. Weber, Elucidating the role of hydroxide electrolyte on anion-exchange-membrane water electrolyzer performance, *J. Electrochem. Soc.* 168 (2021) 054522, <https://doi.org/10.1149/1945-7111/ac0019>.
- [88] D. Li, I. Matanovic, A.S. Lee, E.J. Park, C. Fujimoto, H.T. Chung, Y.S. Kim, Phenyl oxidation impacts the durability of alkaline membrane water electrolyzer, *ACS Appl. Mater. Interfaces* 11 (2019) 9696–9701, <https://doi.org/10.1021/acsami.9b00711>.
- [89] I. Matanovic, Y.S. Kim, Electrochemical phenyl oxidation: a limiting factor of oxygen evolution reaction in water electrolysis, *Curr. Opin. Electrochem.* (2023) 111245, <https://doi.org/10.1016/j.coelec.2023.101218>.
- [90] A. Capri, I. Gatto, C. Lo Vecchio, V. Baglio, Effect of the calcination temperature on the characteristics of Ni/Fe-oxide electrocatalysts for application in anion exchange membrane electrolyzers, *Ind. Chem. Mater.* 1 (2023) 553–562, <https://doi.org/10.1039/d3im00065f>.
- [91] A. Capri, I. Gatto, C. Lo Vecchio, S. Trocino, A. Carbone, V. Baglio, Anion exchange membrane water electrolysis based on nickel ferrite catalysts, *ChemElectroChem* 10 (2023), <https://doi.org/10.1002/celec.202201056>.
- [92] T.Y. Wei, C.H. Chen, K.H. Chang, S.Y. Lu, C.C. Hu, Cobalt oxide aerogels of ideal supercapacitive properties prepared with an epoxide synthetic route, *Chem. Mater.* 21 (2009) 3228–3233, <https://doi.org/10.1021/cm9007365>.
- [93] M. Thommes, K. Kaneko, A.V. Neimark, J.P. Olivier, F. Rodriguez-Reinoso, J. Rouquerol, K.S.W. Sing, Physisorption of gases, with special reference to the evaluation of surface area and pore size distribution (IUPAC Technical Report), *Pure Appl. Chem.* 87 (2015) 1051–1069, <https://doi.org/10.1515/pac-2014-1117>.
- [94] A. Esmaeilifar, S. Rowshanzamir, M.H. Eikani, E. Ghazanfari, Synthesis methods of low-Pt-loading electrocatalysts for proton exchange membrane fuel cell systems, *Energy* 35 (2010) 3941–3957, <https://doi.org/10.1016/j.energy.2010.06.006>.
- [95] C. Wang, G. Wang, D. van der Vliet, K.C. Chang, N.M. Markovic, V. R. Stamenkovic, Monodisperse Pt<sub>3</sub>Co nanoparticles as electrocatalyst: The effects of particle size and pretreatment on electrocatalytic reduction of oxygen, *Phys. Chem. Chem. Phys.* 12 (2010) 6933–6939, <https://doi.org/10.1039/c000822b>.
- [96] J.F. Moulder, W.F. Stickle, P.E. Sobol, K.D. Bomben, Handbook of X-ray Photoelectron Spectroscopy, Perkin-Elmer Corporation, Eden Prairie, MN, USA, 1992. <https://doi.org/10.1002/0470014229.ch22>.
- [97] M.C. Biesinger, B.P. Payne, L.W.M. Lau, A. Gerson, R.S.C. Smart, X-ray photoelectron spectroscopic chemical state Quantification of mixed nickel metal, oxide and hydroxide systems, *Surf. Interface Anal.* 41 (2009) 324–332, <https://doi.org/10.1002/sia.3026>.
- [98] Z.Y. Wu, C.M. Liu, L. Guo, R. Hu, M.I. Abbas, T.D. Hu, H.B. Xu, Structural characterization of nickel oxide nanowires by x-ray absorption near-edge structure spectroscopy, *J. Phys. Chem. B* 109 (2005) 2512–2515, <https://doi.org/10.1021/jp0466183>.
- [99] B.M. Hunter, N.B. Thompson, A.M. Müller, G.R. Rossman, M.G. Hill, J.R. Winkler, H.B. Gray, Trapping an Iron(VI) water-splitting intermediate in nonaqueous media, *Joule* 2 (2018) 747–763, <https://doi.org/10.1016/j.joule.2018.01.008>.
- [100] H. Miyamoto, T. Shinjo, Y. Bando, T. Takada, Mössbauer Effect of Fe<sup>57</sup> in Fe(OH)<sub>2</sub>, *J. Phys. Soc. Jpn.* 23 (1967) 1421.
- [101] S. Bocquet, R.J. Pollard, J.D. Cashion, Dynamic magnetic phenomena in fine-particle goethite, *Phys. Rev. B* 46 (1992) 11657–11664, <https://doi.org/10.1103/PhysRevB.46.11657>.
- [102] P. Axmann, O. Glemser, Nickel hydroxide as a matrix for unusual valencies: the electrochemical behaviour of metal(III)-ion-substituted nickel hydroxides of the pyroaurite type, *J. Alloy. Compd.* 246 (1997) 232–241, [https://doi.org/10.1016/S0925-8388\(96\)02479-6](https://doi.org/10.1016/S0925-8388(96)02479-6).
- [103] J.M.P. Martinez, E.A. Carter, Noninnocent influence of Host β-NiOOH redox activity on transition-metal dopants' efficacy as active sites in electrocatalytic water oxidation, *ACS Catal.* 10 (2020) 2720–2734, <https://doi.org/10.1021/acscatal.9b05092>.
- [104] C.R.H. Bahl, M.F. Hansen, T. Pedersen, S. Saadi, K.H. Nielsen, B. Lebech, S. Mørup, The magnetic moment of NiO nanoparticles determined by Mössbauer spectroscopy, *J. Phys. Condens. Matter* 18 (2006) 4161–4175, <https://doi.org/10.1088/0953-8984/18/17/005>.
- [105] Q. Hu, Y. Xue, J. Kang, I. Scivetti, G. Teobaldi, A. Selloni, L. Guo, L.M. Liu, Structure and oxygen evolution activity of β-NiOOH: where are the protons? *ACS Catal.* 12 (2022) 295–304, <https://doi.org/10.1021/acscatal.1c04647>.
- [106] M.J. Natan, D. Belanger, M.K. Carpenter, M.S. Wrighton, pH-Sensitive Ni(OH)<sub>2</sub>-based microelectrochemical transistors, *Phys. Chem.* 91 (1987) 1834–1842.
- [107] Y.F. Li, J.L. Li, Z.P. Liu, Structure and catalysis of NiOOH: recent advances on atomic simulation, *J. Phys. Chem. C* 125 (2021) 27033–27045, <https://doi.org/10.1021/acs.jpcc.1c06170>.